

A CO survey in planet-forming disks: characterizing the gas content in the epoch of planet formation

A.S. Hales^{1,2}, I. De Gregorio-Monsalvo^{1,3}, B. Montesinos⁴, S. Casassus⁵, W.F.R. Dent^{1,3},
C. Dougados⁶, C. Eiroa⁷, A.M. Hughes⁸, G. Garay⁵, D. Mardones⁵, F. Ménard⁶,
Aina Palau⁹, S. Pérez⁵, N. Phillips^{1,3}, J.M. Torrelles¹⁰ and D. Wilner¹¹

¹Atacama Large Millimeter/Submillimeter Array, Joint ALMA Observatory, Alonso de Córdova 3107, Vitacura 763-0355, Santiago - Chile

²National Radio Astronomy Observatory, 520 Edgemont Road, Charlottesville, Virginia, 22903-2475, United States

³European Southern Observatory, Karl-Schwarzschild-Str. 2, 85748, Garching bei München, Germany

⁴Department of Astrophysics, Centre for Astrobiology (CAB, CSIC-INTA), ESAC Campus, P.O. Box 78, 28691 Villanueva de la Cañada, Madrid, Spain

⁵Departamento de Astronomía, Universidad de Chile, Camino El Observatorio 1515, Las Condes, Santiago, Chile

⁶UMI-FCA, CNRS/INSU, France (UMI 3386), and Dept. de Astronomía, Universidad de Chile, Santiago, Chile.

⁷Departamento de Física Teórica, Facultad de Ciencias, Universidad Autónoma de Madrid, Cantoblanco, 28049, Madrid, Spain

⁸Department of Astronomy, University of California, Berkeley, CA 94720, USA

⁹Institut de Ciències de l'Espai (CSIC-IEEC), Campus UAB-Facultat de Ciències, Torre C5-parell 2, 08193 Bellaterra, Catalunya, Spain

¹⁰Institut de Ciències de l'Espai (CSIC-IEEC) and Institut de Ciències del Cosmos (UB-IEEC), Martí i Franquès 1, 08028 Barcelona, Spain

¹¹Harvard-Smithsonian Center for Astrophysics, Cambridge, MA 02138, USA

– 2 –

ahales@alma.cl

Received _____; accepted _____

Accepted for publication in the Astronomical Journal

ABSTRACT

We carried out a $^{12}\text{CO}(3-2)$ survey of 52 southern stars with a wide range of IR excesses (L_{IR}/L_*) using the single dish telescopes APEX and ASTE. The main aims were (1) to characterize the evolution of molecular gas in circumstellar disks using L_{IR}/L_* values as a proxy of disk dust evolution, and (2) to identify new gas-rich disk systems suitable for detailed study with ALMA. About 60% of the sample (31 systems) have $L_{\text{IR}}/L_* > 0.01$ typical of T-Tauri or Herbig AeBe stars, and the rest (21 systems) have $L_{\text{IR}}/L_* < 0.01$ typical of debris disks. We detect CO(3-2) emission from 20 systems, and 18 (90%) of these have $L_{\text{IR}}/L_* > 0.01$. However, the spectra of only four of the newly detected systems appear free of contamination from background or foreground emission from molecular clouds. These include the early-type stars HD 104237 (A4/5V, 116 pc) and HD 98922 (A2 III, 507 pc, as determined in this work), where our observations reveal the presence of CO-rich circumstellar disks for the first time. Of the other detected sources, many could harbor gaseous circumstellar disks, but our data are inconclusive. For these two newly discovered gas-rich disks, we present radiative transfer models that simultaneously reproduce their spectral energy distributions and the $^{12}\text{CO}(3-2)$ line profiles. For both of these systems, the data are fit well by geometrically flat disks, placing them in the small class of non-flaring disks with significant molecular gas reservoirs.

Subject headings: circumstellar matter – planetary systems: protoplanetary disks

1. Introduction

Most stars are born surrounded by massive circumstellar disks of dust and gas ($M_{\text{disk}} \sim 10^{-3} - 10^{-1} M_{\odot}$; Williams & Cieza 2011). As the systems evolve the disks fade, most of the circumstellar material is accreted either into the central star, into km-size bodies, or dissipated by other gas dispersal mechanisms (Hollenbach et al. 2000; Alexander 2013). Models predict that most gas dissipates quickly after the star is formed ($t < 10$ Myr; Boss 2001), while the combined effects of collisional grinding of large bodies together with gravitational resonances can maintain a significant dust grain population for several Myr ($t < 1$ Gyr; Wyatt 2008). The fraction of stellar flux re-radiated by the dust (the disk-to-star bolometric luminosity ratio, L_{IR}/L_* , also referred as the infrared excess) is a function of the dust mass present in the disk. $L_{\text{IR}}/L_* > 10^{-1}$ in young T Tauri and Herbig Ae/Be (HAeBe) stars with massive circumstellar disks, while in more evolved debris disk systems $L_{\text{IR}}/L_* < 10^{-3}$ (Zuckerman 2001). Observations indicate that warm ($T > 100$ K) dust located in the disk inner regions ($r < 10$ AU) decays with time as t^{-1} (Rieke et al. 2005; Meyer et al. 2007), as expected from steady-state collisional evolution models of the dust particles (i.e. the observed dust is secondary; Wyatt et al. 2007), although there are individual systems with luminosities in excess of steady-state predictions (e.g. η Corvi; Wyatt et al. 2005).

The gas content of protoplanetary disks is more difficult to probe than dust. The zero dipole moment of the most abundant gaseous molecule, H_2 , hampers its observation. The second most abundant molecule, carbon monoxide (CO), has a large dipole moment but its observation in circumstellar disks is very often contaminated by large scale emission, particularly when observed at low angular resolution (Dent et al. 2005; van Kempen et al. 2007). This is unfortunate, as the gas dominates the disk dynamics in the early protoplanetary stages. The gas-to-dust ratio affects the thermal and chemical balance

(Jonkheid et al. 2007; Woitke et al. 2009), as well as the dynamic coupling of gas and dust (Weidenschilling 1977; Takeuchi & Artymowicz 2001). The gas temperature determines the scale height of the disk (D’Alessio et al. 1999, 2006), and most importantly, the mechanisms of gas dispersal will set the timescales for the formation of gas-giant planets (Armitage 2011). Consequently, in the field of planet formation much effort is currently aimed at constraining the timescales over which most circumstellar gas dissipates (e.g., Carmona 2010; Ingleby et al. 2011; Williams & Cieza 2011).

Dynamical instability models predict the formation giant planets on orbital timescales ($t \ll 1$ Myr;; Boss 2005), while core accretion models require at least a few Myr to form Jovian planets (Pollack et al. 1996). These ages are similar to the age of most T Tauri and HAeBe systems. Large amounts of molecular and atomic gas emission are indeed detected towards such objects (Dutrey et al. 1996; Dunkin et al. 1997; Thi et al. 2001), but these signatures disappear towards systems with lower L_{IR}/L_* values (Zuckerman et al. 1995; Dent et al. 2005; Moór et al. 2011). Dent et al. (2005) carried out a sub-mm survey for CO emission in a sample of 59 objects with a variety of L_{IR}/L_* values, classified as either T Tauri and HAeBe stars or more evolved debris disk-like systems. They found that CO detections are common in objects with $L_{\text{IR}}/L_* > 0.01$, but rare in objects with smaller values ($< 10\%$ of these objects). Optical searches for atomic gas over samples with wide range of L_{IR}/L_* also indicate that atomic emission lines originating close to the stars disappear in stars with $L_{\text{IR}}/L_* < 0.01$ (Dunkin et al. 1997; Redfield et al. 2007), suggesting a possible transition from gas-rich to gas-depleted disk near $L_{\text{IR}}/L_* \sim 0.01$. However, less than 5% of known HAeBe and debris disks like systems have been surveyed for gas in either CO or optical emission lines (Thé et al. 1994; Rhee et al. 2007a), hampering robust statistical conclusions.

A few $L_{\text{IR}}/L_* \sim 10^{-3} - 10^{-4}$ systems still show signatures of circumstellar gas, either

in the form of CO emission-line profiles associated with orbiting gas (Zuckerman et al. 1995; Dent et al. 2005; Pascucci et al. 2006; Moór et al. 2011) or by showing sharp optical absorption features at the core of photospheric lines, attributable to circumstellar gas around these stars, in the form of shells, clumps or possibly edge-on disks (Dunkin et al. 1997; Redfield et al. 2007). These systems have become of great interest, as they are thought to be objects transitioning between their protoplanetary and debris disk phase, close to the end of planet formation. Hughes et al. (2008b) conducted submillimeter observations of one of these systems, the A1V star 49 Cet, which revealed a CO gas disk with a depleted inner region, similar to the structures predicted by planetary formation and photo-evaporation models (Armitage 2011; Owen et al. 2012). Another interesting 49 Ceti-like system is HD 21997 (Moór et al. 2011), for which Kospal et al. (2013) recently obtained ALMA observations. The origin of the gas observed in these systems is still a matter of debate, as it is not yet clear whether it is primordial (left from the protoplanetary phase), or secondary (created by collisions and/or photodesorption from dust grains, e.g. Zagorovsky et al. 2010).

In this work we present a survey for ^{12}CO ($J=3-2$) gas over a sample of 52 southern stars with circumstellar dust excesses selected from the literature (Thé et al. 1994; Malfait et al. 1998; Mannings & Barlow 1998; Silverstone 2000), by using the APEX and ASTE submillimeter telescopes. These two telescopes were the best southern facilities to provide bona-fide disk detections in the pre-ALMA era, despite lack of high spatial resolution and sensitivity. By targeting stars with a range of L_{IR}/L_{\star} we aim at studying the dependence between L_{IR}/L_{\star} and detectability of CO. No systematic southern surveys for CO gas in protoplanetary disks have been carried out to date. Nyman et al. (1992) used SEST to observe bright southern IRAS sources, most of which were evolved objects, such as AGB, post-AGB and carbon stars. Recently Moór et al. (2011) conducted a CO search over a sample of 20 southern debris disks systems, leading to the detection of the gas-rich

debris disk system HD 21997, similar to 49 Cet. A southern survey is necessary not only to complement results from northern CO surveys (Zuckerman et al. 1995; Greaves et al. 2000; Dent et al. 2005; Liu et al. 2011) but also to provide a sample of gas-rich southern protoplanetary disks that can be targeted for high-resolution studies with ALMA. Follow-up high-resolution, high-sensitivity ALMA observations of other gas tracers can be used to constrain the physico-chemical structure of the newly discovered disks, as well as to test models predictions in which certain molecular species will be subject to significant radial gradients and differentiation (e.g., Walsh et al. 2010).

In Section 2 we present our target selection. Section 3 describes our observations and data reduction. Our main results are shown in Section 4. Detailed radiative transfer modelling of two of the CO-rich objects, HD 104237 and HD 98922, is presented in Section 5. In Section 6 we discuss our results and in Section 7 we conclude. Appendix A presents individual sources with contaminated CO detections.

2. The sample

Our target sample consists of 52 protoplanetary and debris disk systems selected from the literature as having infrared excesses due to orbiting dust (Thé et al. 1994; Malfait et al. 1998; Mannings & Barlow 1998; Silverstone 2000; Sylvester & Mannings 2000). The targets were selected in terms of their photospheric emission line characteristics (presence or absence of H_α , i.e. T Tauri/HAeBe versus debris disk), isolation from molecular clouds and from bright 2MASS sources, and particularly their L_{IR}/L_* values. Most stars located close to the galactic plane ($|b| < 5$) were avoided in order to minimize cloud contamination in the off- position. We included most southern HAeBe stars from Malfait et al. (1998), and several southern debris disk systems with $L_{\text{IR}}/L_* > 10^{-4}$ from the compilation of Silverstone (2000) and Rhee et al. (2007a). The sample comprised

isolated HAeBe and debris disk systems to study the evolution of the gaseous component of their protoplanetary/debris disks. The sources of our sample were selected based on different ratios of the infrared excess flux to the photospheric flux L_{IR}/L_* , as a proxy of the evolutionary status of the disks. We covered a range of L_{IR}/L_* that varies from several orders of magnitude, ranging from 10^{-5} to close to unity. We did not consider objects younger than 10^6 years nor embedded objects, to avoid contamination from protostellar envelopes or from molecular cloud material. Thus, with these proposed ‘naked’ disks, we expect to reduce the possibility of CO contamination by their parental clouds. Table 1 lists our targets, their spectral types and distances, as well as their L_{IR}/L_* values.

The L_{IR}/L_* values listed in Table 1 were taken from the literature (Acke & van den Ancker 2004; Meeus et al. 2012), when available, or by fitting black-bodies to published optical, infrared and sub-mm data from the literature. The observed SEDs are assumed to be the sum of the model stellar atmosphere SED (SED_*) and a cooler black body of a given temperature (SED_{disk}), i.e. $\text{SED}_{\text{tot}} = \text{SED}_* + \text{SED}_{\text{disk}}$. For each stars in Table 1, we searched for the model that minimised the chi-squared (χ^2) difference between the modelled SED_{tot} and the observed data-points. The search was performed using the variable-metric routine Migrad of the Minuit package from CERN¹. The photospheric luminosities (SED_*) were computed from stellar model atmospheres (assuming spectral types listed in SIMBAD), which were reddened to match the optical data. A value of $R_V = 3.1$ was assumed. It is well known that the blue and ultraviolet regions of the spectrum are the ones most affected by extinction, therefore, when available, ultraviolet spectra obtained with the *IUE* (International Ultraviolet Explorer; Boggess et al. 1978) observatory were added to the SED; they were extremely useful in many cases to estimate $E(B - V)$. L_{IR}/L_* was then

¹<http://seal.web.cern.ch/seal/work-packages/mathlibs/minuit/home.html>

obtained by fitting black-body laws to the infrared excess. In some cases two black-bodies were required in order to fit both the near-IR and far-IR excesses. We estimate our method to be accurate by factors of 2-3 by comparing our L_{IR}/L_* results with stars with values already published in the literature (Sylvester & Mannings 2000; Meeus et al. 2012). Example results from our SED fitting method are shown in Figure 1.

In our sample 59.6 % of the sources have L_{IR}/L_* values typical of HAeBe and T Tauri stars (> 0.01 , for which Dent et al. (2005) find a 48% CO detection rate). The other 40.4 % of the objects have $L_{\text{IR}}/L_* < 0.01$ and have been selected in order to characterize the transition zone where gas-rich to gas-depleted disks is thought to occur ($L_{\text{IR}}/L_* \sim 0.01$; Dent et al. 2005). The Herbig Ae star HD 100546, known to harbor a CO-rich protoplanetary disk, was also included in the sample as a control target (Panić et al. 2010).

3. Observations and data reduction

Here we describe the main $^{12}\text{CO}(3-2)$ single dish survey, and complementary far-infrared and submillimeter line and continuum observations of a few of the detected sources.

3.1. ASTE and APEX $^{12}\text{CO}(3-2)$ observations

Observations were carried out using the Atacama Submillimeter Telescope Experiment (ASTE; Kohno 2005) and the Atacama Pathfinder Experiment² (APEX; Güsten et al.

²Based on observations with the Atacama Pathfinder Experiment (APEX) telescope. APEX is a collaboration between the Max Planck Institute for Radio Astronomy, the European Southern Observatory, and the Onsala Space Observatory.

2006), both located at 5000 m above sea level in the Atacama Desert. Spectra towards each star were acquired using the standard on-off observing pattern to remove atmospheric continuum emission, using typical beam-switching offsets of 180 arcseconds in azimuth. In cases where spurious absorption lines were seen in the spectra due to ambient emission in the off- position, a second observation using an off- position of -180 arcseconds in azimuth was obtained. Spectral line observations of the J=3-2 transition of ^{12}CO (rest frequency $\nu = 345.795991$ GHz) were made using the 2-SB 350 GHz receiver on ASTE and the SHeFI 345 GHz receiver on APEX. The velocity resolution on ASTE and APEX was of 0.5 km s^{-1} and 0.4 km s^{-1} , respectively. The total bandwidths covering the ^{12}CO line were 1 GHz and 0.5 GHz for APEX and ASTE respectively. The beam widths of APEX and ASTE at this frequency were 18 and 21 arcseconds, respectively. Typical disk sizes for protoplanetary disks are a few hundred AU, and will therefore be unresolved in our observations. The corresponding main beam efficiencies (η_{mb}) listed in the ASTE³ and APEX⁴ instrument webpages are 0.6 and 0.73.

In order to reach a targeted root-mean-square (RMS) noise level of $0.02 - 0.04 \text{ K}$ (comparable to the northern survey of Dent et al. 2005), typical integration times of 1 and 2 hours were required for APEX and ASTE, respectively. The survey was completed in different observing blocks during June 2008, July 2009, December 2009, and July 2010 (APEX Project Codes C-081.F-0010B, C-083.F-0187A, and C-084.F-0478A). The precipitable water vapour was typically between 1mm and 2mm, with exceptionally good conditions ($0.3 - 0.9 \text{ mm}$) encountered during the July 2010 run. Close to 80 hours of telescope time were required for completing the survey.

³<http://www.nro.nao.ac.jp/~aste/cfp2011/note.html>

⁴<http://www.apex-telescope.org/telescope/efficiency/>

The ASTE spectra were converted to FITS format using the Newstar package⁵. After conversion to FITS, both the ASTE and APEX spectra were processed using the GILDAS/CLASS reduction software (Guilloteau & Lucas 2000)⁶. The raw data individual scans were visually inspected for identifying spikes, outliers, and baselines instabilities. Scans with problems were excluded from the data reduction. A baseline subtraction from each individual scan was performed excluding channels that showed spectral emission line. A polynomial of degree three or less was used for the baseline fitting. In order to produce the final spectra with the highest signal-to-noise ratio, scans were averaged. The rms noise was computed in the averaged spectra excluding the channels that contained signal from the object of interest.

The 2008 ASTE data were affected by an instrumental 1 MHz sinusoidal ripple of variable amplitude and phase. This artifact was removed from each individual 10 s integration by fitting the first peak of the spectrum’s Fourier components and subtracting it (Hughes et al. 2010, for details).

3.2. LABOCA Archive observations

An 870 μm continuum map of the HD 104237 system obtained with the LABOCA bolometer array camera on APEX (Siringo et al. 2009) was retrieved from the ESO archive⁷ (PI R. Liseau, project code 082.F-9304A). The observations were performed on 28 December 2008 in stable conditions with line-of-sight $\tau = 0.38$, using a standard compact raster of spiral scan pattern which yields excellent spatial sampling. Instrumental sensitivity, as

⁵<http://www.nro.nao.ac.jp/~nro45mrt/obs/newstar/>

⁶<http://www.iram.fr/IRAMFR/GILDAS/doc/html/class-html/class.html>

⁷<http://archive.eso.org>

determined by flux calibrator measurements, was reduced to approximately 64% of nominal this night due to a bias problem. The data were scaled to compensate for this in the reduction, but the noise is accordingly increased.

Data were reduced using a custom pipeline in the BoA package^{7 8}. The pre-processing steps consisted of flagging dead or cross-talking channels, frames with too high telescope accelerations and with unsuitable mapping speed, as well as temperature drift correction using two blind bolometers. Data reduction process included flat-fielding, opacity correction, calibration, correlated noise removal (atmospherics fluctuations seen by the whole array, as well as electronic noise originated in groups of detector channels), and de-spiking. Every scan was visually inspected to identify and discard corrupted data. The final map shows an angular resolution of 19" and an RMS noise of 18 mJy/beam (calculated in the central part of the map).

3.3. *Herschel*/PACS Archive Observations

We have analysed unpublished *Herschel* observations of HD 98922 using the PACS instrument in both photometric and spectroscopic modes that exist in the *Herschel* Science Archive (Pointed Range Spectroscopy observing mode). We used the Level 2 archived standard products produced by the *Herschel* Standard Product Generation (SPG) software, version 10.3.0. PACS photometry was extracted by PSF fitting to obtain 70 and 160 μm fluxes (3815.2 877.5 Jy respectively). The RMS in the 70 and 160 μm maps are 0.2 and 0.4 mJy/pixel respectively. The uncertainty in the derived fluxes will be dominated by the 5% absolute calibration accuracy of PACS (Balog et al. 2013), so we quote 5% photometric errors for the PACS final fluxes in Table 4.

⁸<http://www.apex-telescope.org/bolometer/laboca/boa/>

4. Results

Figure 3 shows the spectra for four detections that appear to be free from foreground/background contamination in the off- spectra. Association of the CO emission to the targeted stars may be determined by comparing the velocity of the detected emission to the velocity of the star determined from optical spectra (the known V_{LSR} velocity of the stars are plotted on top of the spectra, when available).

Integrated line intensities on the detections, or $1\text{-}\sigma$ upper limits, are presented in Table 1 in antenna temperature units. Upper limits were computed as $T_{rms}\Delta v\sqrt{N}$, where T_{rms} is the noise measured in the spectra, Δv is the velocity resolution of each channel, and N is the number of channels over a 10 km s^{-1} velocity interval. We report an integrated CO intensity of $2.5 \pm 0.3\text{ K km s}^{-1}$ (T_A^*) towards our control target HD 100546, compared to the previously measured $2.9 \pm 0.4\text{ K km s}^{-1}$, which are consistent within the uncertainties. (also in T_A^* ; Panić et al. 2010).

A single-dish non-detection of CO implies that neither a CO disk nor CO ambient emission is detected towards the targeted star (fainter CO disk could be present below the sensitivity limit).

However, a CO detection does not necessarily mean that a gaseous disk is present. van Kempen et al. (2007) already noted the difficulty of disentangling ambient CO emission versus protoplanetary disk signatures when looking for circumstellar CO using a single-dish telescopes towards pre-MS stars in Lupus. While most debris disk systems are isolated from molecular clouds, younger stars are usually still associated to their parent clouds (see Figure 2), increasing the probability of contamination from ambient CO in the spectra (either in the off-, the on- position, or both), and need interferometric observations to filter

out the extended cloud emission.

We surveyed 52 stars for $^{12}\text{CO}(3-2)$ emission and obtained detections towards 20 objects. 18 (90%) of the detected sources have $L_{\text{IR}}/L_* > 0.01$. This trend is in agreement with the findings of the survey from Dent et al. (2005) in which $\sim 50\%$ of the systems with $L_{\text{IR}}/L_* > 0.01$ have significant CO detections. Our statistics are, however, biased due to cloud contamination toward many of the sources. The description of the individual sources and results with detections with background/foreground contamination is given in Appendix A.

4.1. ^{12}CO Disk detections

4.1.1. HD 104237

HD 104237 (DX Cha) is the only early-type star of the young ϵ Cha cluster (3 – 5 Myr; Feigelson et al. 2003). It is a Herbig Ae star (A4Ve-A8Ve; Grady et al. 2004; Lyo et al. 2008) with infrared excess (Walker & Wolstencroft 1988; Hu et al. 1989). At least five stars are found within 15 arcseconds of HD 104237, labeled with letters from "B" to "E" (Feigelson et al. 2003). They are lower-mass stars of which at least two have IR excesses and emission lines, associated to T Tauri type stars (Grady et al. 2004). Optical spectroscopy has revealed that HD 104237 is actually a close binary system, where the secondary is a K3 star (HD 104237-2) at ~ 0.2 AU (Böhm et al. 2004). Model fits to its SED suggest that HD 104237 is surrounded by a dust disk with an irradiated inner wall that shadows the outer disk (Meeus et al. 2001). Very Large Telescope (VLT) AMBER observations resolve the inner radius of the ring at $R \sim 0.45$ AU (Tatulli et al. 2007; Garcia et al. 2013). The binary separation $a = 0.22$ AU implies the disk is circumbinary (Böhm et al. 2004).

HD 104237 belongs to a small group SED-predicted flat disk sources that exhibit moderate [O I] emission at optical wavelengths (Acke et al. 2005). Recent modeling of the optical to mid-infrared SED by Fang et al. (2013) supports Meeus et al. (2001) SED interpretation of HD 104237's being surrounded by a self-shadowed (i.e. non-flared) dust disk (therefore being a Group II source according to the classification of Meeus et al. 2001).

There is evidence of circumstellar gas around HD 104237 detected in the Br γ line (Kraus et al. 2008), and marginally detected in the optical [O I] 6300 Å line (the detection is contaminated by photospheric absorption; Acke et al. 2005). While an [O I] emission could arise from warm surface layers of an orbiting gas disk, the hydrogen Br γ emission appears to come from a gaseous inner (< 1 AU) disk (Kraus et al. 2008). Garcia et al. (2013) suggest, from recent VLT data, that Br γ is actually very compact and mostly arises from the close environment of each component of the binary, probably related to accretion flows. However, these findings are derived from interferometric observations that filter out any component extended over scales larger than a few AUs. No H $_2$ emission was detected in the pure rotational line in the mid-IR (Carmona et al. 2008). Meeus et al. (2012) detected strong [O I] 63.2 μm emission towards the HD 104237 using PACS on the *Herschel Space Telescope*, indicating that there are significant amounts of circumstellar gas around this system. A large-scale jet elongated in the southeast-northwest directions and seen in Ly α originates from this source (Grady et al. 2004).

A double-peaked CO line profile is detected in the ASTE spectrum (Figure 3), centered at 5 km s $^{-1}$ and of roughly 8-9 km s $^{-1}$ width. HD 104237 is located in a region between the Cha II and Cha I clouds, at the edge of Cha II. The NANTEN $^{12}\text{CO}(1-0)$ map (Mizuno et al. 2001) shows ambient emission close to the HD 104237 system in the 2-6 km s $^{-1}$ range. The stellar velocity plotted on top of the spectrum was obtained from Gontcharov (2007). The CO emission is centered at the star's position (confirmed by

spectra with different off-positions) , indicating that the disk contribution dominates the ambient cloud contribution.

4.1.2. HD 98922

Together with HD 104237, HD 98922 is also member of the small groups flat-disk sources with [O I] emission at optical wavelengths (Acke et al. 2005). No H₂ emission was detected in the pure rotational line in the mid-IR (Martin-Zaïdi et al. 2008). Similarly to HD 104237, the 63.2 μm [O I] line is also detected (Fedele et al. 2013).

A single-peaked profile is detected in CO(3-2) towards HD 98922 (Figure 3), centered at -7 km s⁻¹. The line velocity is offset by 15 km s⁻¹ from the radial velocity listed in Acke et al. (2005). This offset is, however, comparable to their centroiding error in the stellar velocity determination (between 8 and -15 km s⁻¹). HD 98922 is located at 7 degrees above the Galactic Plane ((*l, b*) = (289.78, +07.21)) in the direction of the Third Quadrant (Dame et al. 2001), but there are no prominent known molecular clouds on the line-of-sight. The two closest clouds derived from extinction maps are located at (*l, b*) = (290.70, 5.83) and (290.93, 7.50) respectively (Dobashi et al. 2005). Since there are no known molecular clouds in the line-of-sight, nor evidence of contamination in the reference spectrum, we associate the CO emission to the stellar position (within the ASTE primary beam).

4.1.3. HD 155448

Classified as a B9-type star, there have been two main interpretations in the literature concerning the nature of HD 155448: it has been proposed to be a HAeBe star with a circumstellar disk (Malfait et al. 1998; Schütz et al. 2004), or a post-AGB star surrounded

by an ejected shell (Luna et al. 2008; Ortiz et al. 2005).

Schütz et al. (2011) seems to have resolved this dichotomy by analysing the system in detail using resolved photometry and spectroscopy. They propose this is actually a quintuple system and rule out a possible post-AGB nature: 4 out of 5 components lie close to the ZAMS in the HR diagram. According to Schütz et al. (2011), the C component presents spectral signatures corresponding to a star with a circumstellar disk.

A single-peaked profile is detected towards HD 155448, centered at 24 km s^{-1} and of roughly 6 km s^{-1} width (Figure 3). Luna et al. (2008) detected optical absorption features of H_α and Carbon at 36 km s^{-1} and 26 km s^{-1} respectively, which they associated to an expanding circumstellar envelope. Even though the expanding post-AGB envelope scenario has been ruled out by Schütz et al. (2011), it is interesting to note that the $^{12}\text{CO}(3-2)$ emission of HD 155448 coincides in velocity with the optical atomic carbon emission detected in Luna et al. (2008).

4.1.4. *RX J1842.9-353*

A double peaked profile characteristic of rotating disks is detected towards RX J1842.9-353 in the ASTE spectrum (Figure 3). The ASTE detection was analyzed alongside complementary SMA data presented in Hughes et al. (2010). In the SMA data the dust disk was detected and marginally spatially resolved, while the CO observations resulted in an interferometric upper limit.

4.2. LABOCA 870 μm continuum map of HD 104237

The LABOCA 870 μm continuum map of HD 104237 (Figure 5) shows a clear detection of the primary disk, but also significant extension to the South-East, consistent with emission from a disk around the D or E components in the system. Based on the mid-IR detection of a disk around the E component by Grady et al. (2004), we have extracted fluxes using a model of two point sources separated by the 14.9'' A-E separation vector (Figure 6). This yielded fluxes of 154 ± 24 mJy and 91 ± 24 mJy for the A and E components respectively (uncertainties allow for S/N, calibration uncertainty and anti-correlated error of the two fluxes), and a position offset error of under 2''. Due to the system configuration, any flux from the D component will mostly be incorporated in the E component flux, and any emission from the B and C components will be included in the A component flux.

5. Radiative transfer modeling of HD 104237 and HD 98922

In this section we use the 3D radiative transfer Monte Carlo code MCFOST (Pinte et al. 2006) to model simultaneously the SEDs and $^{12}\text{CO}(3-2)$ spectra of two of the four sources exhibiting emission from a disk and not contaminated by known molecular clouds. We model only two sources, HD 104237 and HD 98922. RX J1842.9-353 is already modeled by Hughes et al. (2010), and given the complexity of the HD 155448 system (Schütz et al. 2011), we do not carry out radiative transfer of this system but do include it in our final detection statistics.

The models presented in this section assume that the dust and gas are well coupled, with a dust-to-gas ratio of 10^{-2} and a 10^{-4} CO abundance with respect to H_2 . The canonical average dust-to-gas ratio found in the literature for the ISM is in the order of 10^{-2} , we assume that young protoplanetary disks should then have similar ratios, although decreasing

as the gas dissipates and dust grains grow (Birnstiel et al. 2010). The relative abundances of CO and H₂ are constant in the diffuse ISM and equal to 10⁻⁴ (Federman et al. 1980; Lee et al. 1996). These standard values for the dust-to-gas and CO/H₂ ratios therefore constitute a first reasonable approach to the true physical properties of the disks.

MCFOST assumes that the gas-dust thermal exchange is perfect and that gas and dust are in local thermodynamic equilibrium (LTE) throughout the disk. The LTE approximation is justified for low-J CO lines, as has been demonstrated several times (Pavlyuchenkov et al. 2007; Panić & Hogerheijde 2009). Freeze out is a natural outcome of a cold media containing dust and gas. It is well known from laboratory and from astronomical data that CO freezes out at ~ 20 K (Qi et al. 2011; de Gregorio-Monsalvo et al. 2103). Models accounting for the freeze-out of CO into dust grains at temperature of ~ 20 K can also be incorporated in MCFOST.

5.1. HD104237 SED and CO disk modeling with MCFOST

Due to its complexity (circumstellar activity, multiplicity), the basic stellar parameters of HD 104237 have been been loosely constrained. There is a large discrepancy in temperature, luminosity of the primary (HD 104237 or HD 104237A hereafter) and the secondary (HD 104237A-2) star (e.g. for the primary $T \sim 7300 - 9550$ K, and $L \sim 20 - 60 L_{\odot}$; Fumel & Böhm 2012). Table 2 summarizes the available photometric data used for the SED modelling of this system. For our SED fitting we adopted the effective temperatures and luminosities from Tatulli et al. (2007), that is $T_{eff,1} = 8000$ K, $L_1 = 30 L_{\odot}$, for the primary and $T_{eff,2} = 4750$ K, $L_2 = 3 L_{\odot}$ for the secondary star. This combination of stellar parameters is able to fit the available optical and *IUE* data (Boggess et al. 1978) with no need of any reddening (Figure 7), and were therefore adopted as the energy source for the radiative transfer modeling. Other parameters such as

stellar masses and stellar radii are taken from Garcia et al. (2013). The fundamental stellar parameters assumed for modeling the energy input of the system are presented in Table 3.

The surface density distribution of the disk that was adopted is the tapered-edge model (Andrews et al. 2009; Williams & Cieza 2011),

$$\Sigma = \Sigma_C \left(\frac{R}{R_C} \right)^{-\gamma} \exp \left[- \left(\frac{R}{R_C} \right)^{2-\gamma} \right] \quad (1)$$

, where Σ_C is the surface density at the characteristic radius R_C , and γ is a variable physically related to the disk’s viscosity (Hughes et al. 2008a). The latter controls the radial variation of the density distribution by providing a power law distribution in the inner disk with an exponential taper in outer regions. The inner rim value of 0.45 AU was adopted from Tatulli et al. (2007). The flaring parameters were also varied, assuming that at a given radius the disk column density is distributed vertically like a Gaussian with a scale-height

$$H = H_C R_C \left(\frac{R}{R_C} \right)^\psi \quad (2)$$

where $H_C R_C$ is the scale height at the characteristic radius R_C , and ψ describes the dust disk flaring. In summary, the total disk mass (M_D , obtained by integrating the entire density distribution), R_C , γ , ψ and h_C (the scale height at the characteristic radius) were variables of the model fitting routine.

The dust grains consist of astronomical silicates and are distributed in size following a power law, $n(a) \propto a^{-3.6}$ between $a_{min} = 0.03 \mu\text{m}$ and $a_{max} = 7000 \mu\text{m}$ (Draine & Lee 1984). Without constraints on the disk sizes (i.e. direct imaging), the fitting process is a highly

degenerate problem: changes in the disk outer radius and the surface density distribution can be made to artificially match the SED and CO data. A range of γ values from 0 to 2 were explored in order to fit the SED data, until a good match was found. A range of disk outer radius from 60 to 120 AU was explored. The disk's total mass was mostly constrained by the long wavelength data points. However, given the uncertainties and assumptions in the models, we did not attempt to optimise these fits any further and therefore no formal errors are quoted in the variable terms. We stress the fact that this model is simply a rough model that matches the data and is by no means a best-fit model in formal terms. The data and is by no means a best-fit model in formal terms.

The SED can be fit with a 90 AU disk of total dust mass $4 \times 10^{-4} M_{\odot}$. The extension of the fitted disk is comparable with the 70 AU disk radius estimated by Grady et al. (2004). The total mass we derive is in agreement with that of Henning et al. (1994), who estimated the mass of the system based on the 1.3 mm data. Fang et al. (2013) estimates a smaller disk masses in their models, but with a smaller wavelength range ($<20 \mu\text{m}$) their SED fits were not sensitive to larger dust grains. No flaring is required to match the SED ($\psi = 0$), in good agreement with previous SED studies of the disk's vertical structure which indicate the disk is not flared (Meeus et al. 2001; Fang et al. 2013). We use this fiducial model to attempt to also reproduce the CO observations.

The degeneracies when mining pure SED modeling lacking resolved images are well known, but nonetheless the SED information and the kinematic information from the gas lines can be used to further constrain the disk geometry (Dent et al. 2005; Panić & Hogerheijde 2009; Hughes et al. 2010). MCFOST uses the radiation and temperature fields (assuming $T_{dust} = T_{gas}$) to compute the level populations of CO (assuming LTE), and to produce line emission surface brightness profiles. We have used a gas-to-dust ratio of 100:1 and abundance of CO of 10^{-4} relative to H_2 , constant throughout the disk.

Grady et al. (2004) estimates a disk inclination angle of 18_{-11}^{+14} degrees. This value was used as initial estimate but was then allowed to vary during the different runs. The velocity field is that of Keplerian rotation with a central object of mass equal to that of the combined binary system ($M_1+M_2=3.6 M_\odot$). The systemic velocity (V_{lsr}) and the inclination of the disk were varied until a good match was found.

We find that the standard model over predicts the flux densities by a factor of 2.5. As discussed in Hughes et al. (2010), there are several ways of reducing the predicted CO intensities without changing the dust distribution. Different CO/H₂ ratios, dust-to-gas ratio, or different gas temperatures would significantly change the observed intensities. By incorporating the freeze-out of CO molecules into dust grains at temperatures below 20 K (that is the abundance of CO drops to zero where $T < 20$ K in the disk), the model images fit the data without the need of changing neither the global abundance of CO/H₂, nor the disk total mass. The parameters that reproduce the CO data (Figure 8) are listed in Table 3.

5.2. HD 98922 SED and CO disk modeling with MCFOST

Contrarily to HD 104237, very little information is available on HD 98922. Together with HD 104237, it is one of the few close-by, southern, flat disks with signs of a rich gas chemistry.

The determination of the parameters for HD 98922 turned out to be a particularly difficult issue. The star is bright ($V \sim 6.8$) and was classified as a B9 Ve (Houk, 1978). Taking the typical absolute magnitude for a B9 V star $M_V = +0.2$, that would imply a distance of about 210 pc, whereas the Hipparcos parallax $\pi = 0.98 \pm 0.39$ mas (van Leeuwen,

2007) puts the star much further, leading to a contradiction.

The spectral type B9 Ve seems to have been used in many subsequent works without revision. Following the hint given by the bad fit of the ultraviolet IUE spectrum using models with $T_{\text{eff}} \simeq 10500$ K, typical of a B9AV, it turns out that a temperature around 9000 K gives more sensible results. Garcia-Lopez et al. (2006) reported a fairly high accretion rate $\log \dot{M}_{\text{acc}} (M_{\odot}/\text{yr}) = -5.76$, so one has to be careful interpreting the UV spectrum.

An UVES/VLT spectrum (Mario van den Ancker, private communication) was used to estimate the stellar gravity, using the width of the Balmer lines, and the metallicity. The conclusion is that a model with $T_{\text{eff}} = 9000$ K, $\log g_* = 3.0$ and $[\text{Fe}/\text{H}] = -0.5$, fits reasonably well the spectrum –and also the SED– of the star. This set of parameters would correspond to a spectral type around A2 III. Typical errors would be ± 250 K in T_{eff} , ± 0.1 dex in $\log g_*$ and ± 0.3 dex in $[\text{Fe}/\text{H}]$. Concerning the metallicity, which is a delicate issue, Folsom et al. (2012) point out the fact that HD 98922 shows suspiciously weak metal lines for their literature temperature, hinting at a potential presence of λ Boo peculiarities. Although that analysis is out of the scope of this work, a fit of the region 6140–6180 Å, which contains three O I (6156.0, 6156.8 and 6158.2 Å) and two Fe II lines shows that whereas the Fe II features are well reproduced with an abundance $[\text{Fe}/\text{H}] = -0.5$, or even lower, the oxygen abundance –scaled to the iron abundance– seems to be much larger.

Figures 9 and 10 show the fits to the ultraviolet and optical observations and the spectral fit to the Balmer lines H δ , H ϵ , H $_8$ – H $_{11}$. Low resolution synthetic spectra from the grid of Castelli-Kurucz and high-resolution synthetic spectra computed using the ATLAS9 and SYNTHE codes by Kurucz (1993) were used.

Using the results from the spectral and SED fits we can obtain an estimate of the distance. The process is explained in detail in Montesinos et al. (2009) and makes use of the position of the star in the HR diagram $\log g_* - \log T_{\text{eff}}$, which can be translated to

a point in the HR diagram $\log L_*/L_\odot - \log T_{\text{eff}}$ to obtain an estimate of the luminosity. Once L_*/L_\odot is known, the distance can be estimated through the expression $L_* = 4\pi F_{\text{phot}} d$ where F_{phot} is the stellar flux observed and can be found by integrating the dereddened photospheric model that was fitted to the photometry.

In the panel on the left hand side of Fig. 11 an HR diagram $\log g_* - \log T_{\text{eff}}$ with the PMS evolutionary tracks from the Yonsei-Yale (Yi et al. 2001) collection for $Z = 0.007$ –which corresponds roughly to $[\text{Fe}/\text{H}] = -0.5$ – has been plotted. The tracks correspond to 4.0, 4.2, 4.4, 4.6, 4.8, 5.0 and 5.2 M_\odot . The point (9000 K, 3.0) is higher than the beginning of the tracks, so, to carry out the estimate we have used instead a slightly higher value of $\log g_*$, namely 3.20. The point (9000 K, 3.20 \pm 0.1) translates to the HR diagram $\log L_*/L_\odot - \log T_{\text{eff}}$, on the right hand side of the figure, to a point with $\log L_*/L_\odot = 2.75 \pm 0.20$, therefore, the luminosity of the star would be $L_*/L_\odot = 562^{+329}_{-208}$. The distance implied is $d = 507^{+131}_{-104}$ pc. From this exercise we can also estimate the mass (around 5 M_\odot), whereas the age seems to be less than 1 Myr.

We must note that the parameters we give in this paper have been estimated under the hypothesis that this star is a single object. A binary scenario has also been proposed for HD 98922 (e.g. Blondel & Djie 2006), which could potentially explain the observed SED, the ultraviolet spectrum, and would place the system further away (beyond 600 pc). This and other possible scenarios for the stellar nature of the HD 98922 system will be deferred to a future publication.

Similarly to the modeling presented for HD 104237 (Section 5.1), we have used the MCFOST radiative transfer code (Pinte et al. 2006) to reproduce both the observed SED and the $^{12}\text{CO}(3-2)$ emission the HD 98922 disk. Photometric data available from the literature is listed in Table 4, together with the PACS photometry was incorporated to our SED fitting. Table 5 shows the disk parameters that reproduce the SED and the CO data.

We find that the SED and CO emission can be fit with dust disk mass $2 \times 10^{-5} M_{\odot}$, of 320 AU in radius. Similarly to HD 104237, no flaring with increasing radius is required to fit the SED. No CO freezout is required to fit the CO spectrum. Since the infrared emission is optically thick, the lack of longer wavelength data makes very difficult to estimate the dust mass. The $^{12}\text{CO}(3-2)$ data alone cannot be used to constrain the total disk mass. It is found to be optically thick in disks, hence tracing the surface temperature and not the underlying density field near the mid plane. Moreover, it depends on many variable parameters such as the assumption of $T_{gas} = T_{dust}$, CO freezout temperatures, the dust to gas ratio, and the CO abundance with respect to H_2 . Longer wavelength follow-up (e.g. sub-mm) is required to further constrain the mass of the disk.

6. Discussion

We surveyed a sample of 52 stars covering a broad range of L_{IR}/L_* values. We detect CO(3-2) emission from 20 systems, and 18 (90%) of these have $L_{\text{IR}}/L_* > 0.01$. This implies that in the 31 systems with $L_{\text{IR}}/L_* > 0.01$, we obtain a detectability rate of 58%. Figure 13 shows the integrated CO intensity versus fractional infrared excess for our targets. We have not included the sources with possible background/foreground cloud contamination, and also removed HD 155448. The CO intensities have been normalized to a distance of 100 pc⁹. Our results are in agreement with the previous northern survey of Dent et al. (2005),

⁹The conversion factors used to convert from Kelvin to Jansky were: 78.3 for ASTE (from T_A^*), 40.6 for APEX (from T_A^*), 18.5 for the JCMT (from T_{mb} , since those are the units listed in Dent et al. (2005), conversion factor obtained from http://docs.jach.hawaii.edu/JCMT/HET/GUIDE/het_guide.ps).

where $\sim 50\%$ of the stars $L_{\text{IR}}/L_* > 0.01$ have CO detections.

Ten objects (42%) deviate from that trend by having $L_{\text{IR}}/L_* > 0.01$ but no detectable CO emission. HD 100453 and HD 95881 have indeed been identified as disks in transition from gas-rich to gas-poor (Collins et al. 2009; Verhoeff et al. 2010). HD 95881 appears to be in a particular transition between a gas-rich flaring disk to gas-poor self-shadowed disk (Verhoeff et al. 2010), which would explain the relatively large infrared excess and the lack of detectable CO. Overall, the results from this and previous surveys indicate that the infrared excess is an indicator for detecting CO gas, in agreement with previous studies that suggest that young stars with large amounts of circumstellar dust emission also hold large reservoirs of circumstellar molecular gas (Dent et al. 2005).

Only four of the newly detected systems are, however, clearly free of CO emission from extended gas associated with ambient molecular cloud material. The contaminated sources may indeed harbor significant quantities of CO, but higher resolution interferometric observation would be needed to filter out any cloud contamination from the disk emission. Alternatively, higher density tracers such as HCO^+ or CN could be considered, as (Guilloteau et al. 2013; de Gregorio-Monsalvo et al. 2103). High density tracers will detect the emission from the disk, while the possible contaminating clouds are not dense enough to be detected in these molecules. This is one of the main results from the pilot programme from Guilloteau et al. (2013). In addition, higher order transition in CO and HCO^+ can also be used to avoid contamination from cold clouds, as the temperatures required to excite these transitions are larger than usually found in molecular clouds (see Section A.2).

Most of the sources showing cloud contamination are all well studied disks known to harbor gas emission (e.g. HD 250550, HD 97048, HD 142527, HD 144668, HD 149914, KK Oph and VV Ser). Our single-dish observations indicate they are still associated to their parent clouds, given the coincidence in position and velocity between the observed

spectra and existing molecular cloud maps.

We detect ^{12}CO around HD 104237 and HD 98922 for the first time, and combine it with SED data to produce disk models. We confirm that geometrically flat disk models can indeed reproduce both the SEDs and CO profiles. The incorporation of CO freezeout is required to account for observed CO intensities of HD 104237, and is expected to play a significant role if according to new models the CO is located closer to the midplane where the temperatures are lower. The $63.2\ \mu\text{m}$ [O I] and the [O I] $6300\ \text{\AA}$ line are also detected in both disks. Meeus et al. (2012) found a strong correlation between $63.2\ \mu\text{m}$ [O I] and $^{12}\text{CO}(3-2)$ in a sample of 20 Herbig Ae/Be stars, but no clear correlation between ^{12}CO and [O I] $6300\ \text{\AA}$. Even though the origin of the [O I] $6300\ \text{\AA}$ line is unclear, it is usually thought to originate in the surface of the disks (Acke et al. 2005), and to trace the inner regions of the disk (1-50 AU; van der Plas et al. 2008). The fact we are indeed detecting both [O I] lines and the $^{12}\text{CO}(3-2)$ may indicate that the $^{12}\text{CO}(3-2)$ emission stems from the warmer layers of the disk, although these lines come from different radii ranges with CO(3-2) being from the most outside ($R \geq 100\ \text{AU}$; e.g. Hughes et al. 2008a).

HD 104237 is part of a multiple system, and our LABOCA imaging shows that at least two sources in the field of view have detectable sub-mm emission. Our SED modelling indicates a total disk mass of $4 \times 10^{-2} M_{\odot}$ around the primary component. We can also use the $870\ \mu\text{m}$ flux to estimate the mass of the disk around component E (which may also include a contribution from component D). Assuming $T \sim 20\ \text{K}$, opacity of $0.35\ \text{m}^2/\text{Kg}$ and 100:1 gas-to-dust (e.g., Andrews & Williams 2005), implies a $0.004 M_{\odot}$ disk mass for component E(+D).

The HD 104237 system bears some striking resemblance to RW Aur. RW Aur A is a very active classical T Tauri driving a powerful optical jet. It is separated by $1.2''$ from RW Aur B, and there is also some suspicion that RW Aur A may have a close companion

(from radial velocity variations). Radio interferometric observations of the ^{12}CO and ^{13}CO lines in RW Aur with the Plateau de Bure interferometer (Cabrit et al. 2006) show that the RW Aur A disk is very compact ($R_{out} \sim 40\text{--}57$ AU) probably due to truncation by RW Aur-B. Despite the truncation, a large scale spiral arm extending over 500 AU was detected in ^{12}CO connecting the RW Aur A and RW Aur B disks, interpreted as tidal disruption of the RW Aur-A disk by the companion, to be searched for in the HD 104237 multiple system.

Based on the $1.26''$ separation between HD 104237A and HD 104237B, (Grady et al. 2004) predicted a tidal truncation outer radius of 38 AU for HD 104237A. This is significantly smaller than the 90 AU characteristic radius we derive from the SED modelling. However the truncation radius prediction is subject to uncertainties on the projected distance, while the outer radius disk estimates is known to be poorly constrained by pure SED fitting. Resolved imaging is required to directly measure the outer truncation radius of the disk.

7. Conclusions

We conducted a single-dish survey for $^{12}\text{CO}(3-2)$ gas in a sample of 52 protoplanetary and debris disks. We report a 58% detection rate in sources with infrared excess fraction larger than 0.01. Most of those detections can, however, be associated with a parent molecular cloud, and therefore can only be considered upper limits to the disk emission. We identify four CO detections that can be explained as arising from circumstellar CO gas. We present the detection of two new gas-rich disks, HD 104237 and HD 98922, and use radiative transfer codes to model their continuum and gas emission. Both disks are unusual, geometrically-flat, CO-rich disks with $63.2 \mu\text{m}$ [O I] and [O I] 6300 \AA line emission. HD 104237 and HD 98922 are unique laboratories to study the extreme of SED-predicted flat disks. Are the SEDs of ‘flat’ disks different to those of ‘flared’ disks because of dust

settling into the mid-plane or are they just smaller in radii? Resolved sub-mm images with existing interferometers (e.g. ALMA) are required to further constrain the physico-chemico structure of these disks and ultimately understand the gas-clearing processes which yield planet formation.

Acknowledgments

We are grateful to Mario van den Ancker and Andre Müller for providing the UVES/VLT spectrum of HD 98922 and for fruitful discussions on the determination of the parameters for this star. Based on observations carried out with the Atacama Pathfinder Experiment telescope (APEX). APEX is a collaboration between the Max-Planck Institut für Radioastronomie, the European Southern Observatory, and the Onsala Space Observatory. AH, SC, FM, SP and WFRD acknowledge support from Millennium Science Initiative, Chilean Ministry of Economy: Nucleus P10-022-F. AP and JMT acknowledge support from MICINN (Spain) AYA2011-30228-C03 grants (co-funded with FEDER funds) AGAUR (Catalonia) 2009SGR1172 grant. The ICC (UB) is a CSIC-Associated Unit through the ICE (CSIC). Finally, we would like to thank our anonymous referee for a very careful and detailed review which we think has improved very significantly our paper.

REFERENCES

- Acke, B., & van den Ancker, M. E. 2004, *A&A*, 426, 151
- Acke, B. and van den Ancker, M. E. and Dullemond, C. P., 2005, *A&A*, 436, 209
- Alexander, R. 2013, arXiv:1308.1791
- Alonso-Albi, T., Fuente, A., Bachiller, R., et al. 2008, *ApJ*, 680, 1289
- Andrews, S. M., & Williams, J. P. 2005, *ApJ*, 631, 1134
- Andrews, S. M., Wilner, D. J., Hughes, A. M., Qi, C., & Dullemond, C. P. 2009, *ApJ*, 700, 1502
- Armitage, P. J. 2011, *ARA&A*, 49, 195
- Balog, Z., Müller, T., Nielbock, M., et al. 2013, *Experimental Astronomy*, 38
- Barbier-Brossat, M., & Figon, P. 2000, *A&AS*, 142, 217
- Beichman, C. A., Neugebauer, G., Habing, H. J., Clegg, P. E., & Chester, T. J. 1988, *Infrared astronomical satellite (IRAS) catalogs and atlases. Volume 1: Explanatory supplement*, 1
- Birnstiel, T., Dullemond, C. P., & Brauer, F. 2010, *A&A*, 513, A79
- Blondel, P. F. C., & Djie, H. R. E. T. A. 2006, *A&A*, 456, 1045
- Böhm, T., Catala, C., Balona, L., & Carter, B. 2004, *A&A*, 427, 907
- Boss, A. P. 2001, *ApJ*, 563, 367
- Boss, A. P. 2005, *ApJ*, 629, 535
- Boggett, A., Carr, F. A., Evans, D. C., et al. 1978, *Nature*, 275, 372

- Brittain, S. D., Simon, T., Najita, J. R., & Rettig, T. W. 2007, *ApJ*, 659, 685
- Cabrit, S., Pety, J., Pesenti, N., & Dougados, C. 2006, *A&A*, 452, 897
- Carmona, A., van den Ancker, M. E., Henning, T., et al. 2008, *A&A*, 477, 839
- Carmona, A. 2010, *Earth Moon and Planets*, 106, 71
- Carmona, A., van der Plas, G., van den Ancker, M. E., et al. 2011, *A&A*, 533, A39
- Carpenter, J. M., Snell, R. L., & Schloerb, F. P. 1995, *ApJ*, 445, 246
- Casassus, S., Hales, A., de Gregorio, I., et al. 2013, *A&A*, 553, A64
- Casassus, S., van der Plas, G., M, S. P., et al. 2013, *Nature*, 493, 191
- Collins, K. A., Grady, C. A., Hamaguchi, K., et al. 2009, *ApJ*, 697, 557
- Coulson, I. M., Walther, D. M., & Dent, W. R. F. 1998, *MNRAS*, 296, 934
- Cutri, R. M., Skrutskie, M. F., van Dyk, S., et al. 2003, *VizieR Online Data Catalog*, 2246,
0
- Dahm, S. E., & Carpenter, J. M. 2009, *AJ*, 137, 4024
- D'Alessio, P., Calvet, N., Hartmann, L., Lizano, S., & Cantó, J. 1999, *ApJ*, 527, 893
- D'Alessio, P., Calvet, N., Hartmann, L., Franco-Hernández, R., & Servín, H. 2006, *ApJ*,
638, 314
- Dame, T. M., Hartmann, D., & Thaddeus, P. 2001, *ApJ*, 547, 792
- Dawson, J. R., Kawamura, A., Mizuno, N., Onishi, T., & Fukui, Y. 2008, *PASJ*, 60, 1297
- De Gregorio-Monsalvo, I., et al., *in preparation*, *A&A*

- Dent, W. R. F., Greaves, J. S., & Coulson, I. M. 2005, MNRAS, 359, 663
- de Winter, D., van den Ancker, M. E., Maira, A., et al. 2001, A&A, 380, 609
- de Zeeuw, P. T., Hoogerwerf, R., de Bruijne, J. H. J., Brown, A. G. A., & Blaauw, A. 1999, AJ, 117, 354
- Dobashi, K., Uehara, H., Kandori, R., et al. 2005, PASJ, 57, 1
- Draine, B. T., & Lee, H. M. 1984, ApJ, 285, 89
- Dunkin, S. K., Barlow, M. J., & Ryan, S. G. 1997, MNRAS, 290, 165
- Dutrey, A., Guilloteau, S., Duvert, G., et al. 1996, A&A, 309, 493
- Fang, M., van Boekel, R., Bouwman, J., et al. 2013, A&A, 549, A15
- Fajardo-Acosta, S. B., Telesco, C. M., & Knacke, R. F. 1998a, AJ, 115, 2101
- Fajardo-Acosta, S. B., Stencel, R. E., & Backman, D. E. 1998b, ApJ, 503, L193
- Fedele, D., Bruderer, S., van Dishoeck, E. F., et al. 2013, A&A, 559, A77
- Federman, S. R., Glassgold, A. E., Jenkins, E. B., & Shaya, E. J. 1980, ApJ, 242, 545
- Feigelson, E. D., Lawson, W. A., & Garmire, G. P. 2003, ApJ, 599, 1207
- Folsom, C.P., Bagnulo, S., Wade, G.A., et al., 2012, MNRAS, 422, 2072
- Fukui, Y., Onishi, T., Abe, R., et al. 1999, PASJ, 51, 751
- Fumel, A. & Böhm, T. 2012, A&A, 540, A108
- Garcia, P. J. V., Benisty, M., Dougados, C., et al. 2013, MNRAS, 430, 1839
- García-López, R., Natta, A., Testi, L., & Habart, E., 2006, A&A, 459, 837

- Gontcharov, G. A. 2007, VizieR Online Data Catalog, 903, 20844
- Guilloteau, S., & Lucas, R. 2000, Imaging at Radio through Submillimeter Wavelengths, 217, 299
- Guilloteau, S., Di Folco, E., Dutrey, A., et al. 2013, A&A, 549, A92
- Güsten, R., Nyman, L. Å., Schilke, P., et al. 2006, A&A, 454, L13
- Grady, C. A., Woodgate, B., Torres, C. A. O., et al. 2004, ApJ, 608, 809
- Greaves, J. S., Coulson, I. M., & Holland, W. S. 2000, MNRAS, 312, L1
- Güsten, R., Baryshev, A., Bell, A., et al. 2008, Proc. SPIE, 7020,
- Hamaguchi, K., Yamauchi, S., & Koyama, K. 2005, ApJ, 618, 360
- Hara, A., Tachihara, K., Mizuno, A., et al. 1999, PASJ, 51, 895
- Harju, J., Haikala, L. K., Mattila, K., et al. 1993, A&A, 278, 569
- Hauck, B., & Mermilliod, M. 1998, A&AS, 129, 431
- Henning, T., Launhardt, R., Steinacker, J., & Thamm, E. 1994, A&A, 291, 546
- Hillenbrand, L. A., Carpenter, J. M., Kim, J. S., et al. 2008, ApJ, 677, 630
- Høg, E., Fabricius, C., Makarov, V. V., et al. 2000, A&A, 355, L27
- Hollenbach, D. J., Yorke, H. W., & Johnstone, D. 2000, Protostars and Planets IV, 401
- Houk, N., 1978, Michigan catalogue of two-dimensional spectral types for the HD stars, VizieR on-line data III/51
- Hu, J. Y., The, P. S., & de Winter, D. 1989, A&A, 208, 213

- Hughes, A. M., Wilner, D. J., Qi, C., & Hogerheijde, M. R. 2008a, ApJ, 678, 1119
- Hughes, A. M., Wilner, D. J., Kamp, I., & Hogerheijde, M. R. 2008b, ApJ, 681, 626
- Hughes, A. M., Andrews, S. M., Wilner, D. J., et al. 2010, AJ, 140, 887
- Ingleby, L., Calvet, N., Hernández, J., et al. 2011, AJ, 141, 127
- Jonkheid, B., Dullemond, C. P., Hogerheijde, M. R., & van Dishoeck, E. F. 2007, A&A, 463, 203
- Juhász, A., Bouwman, J., Henning, T., et al. 2010, ApJ, 721, 431
- Kohn, K. 2005, The Cool Universe: Observing Cosmic Dawn, 344, 242
- Kospal, A. et al., *submitted*, 2013
- Kraus, S., Hofmann, K.-H., Benisty, M., et al. 2008, A&A, 489, 1157
- Kun, M., Vinkó, J., & Szabados, L. 2000, MNRAS, 319, 777
- Kurucz, R.L., 1993, ATLAS9 Stellar Atmosphere Programs and 2 km/s grid. CD-ROM No. 13. Cambridge, Massachusetts, Smithsonian Astrophysical Observatory
- Lee, H.-H., Bettens, R. P. A., & Herbst, E. 1996, A&AS, 119, 111
- Liu, T., Zhang, H., Wu, Y., Qin, S.-L., & Miller, M. 2011, ApJ, 734, 22
- Luna, R., Cox, N. L. J., Satorre, M. A., et al. 2008, A&A, 480, 133
- Lyo, A.-R., Lawson, W. A., & Bessell, M. S. 2008, MNRAS, 389, 1461
- Malfait, K., Bogaert, E., & Waelkens, C. 1998, A&A, 331, 211
- Mannings, V., & Barlow, M. J. 1998, ApJ, 497, 330

- Martin-Zaïdi, C., van Dishoeck, E. F., Augereau, J.-C., Lagage, P.-O., & Pantin, E. 2008, *A&A*, 489, 601
- Martin-Zaïdi, C., Habart, E., Augereau, J.-C., et al. 2009, *ApJ*, 695, 1302
- Meeus, G., Waters, L. B. F. M., Bouwman, J., van den Ancker, M. E., Waelkens, C. and Malfait, K., 2001, *A&A*, 365, 476
- Meeus, G., Montesinos, B., Mendigutía, I., et al. 2012, *A&A*, 544, A78
- Meyer, M. R., Backman, D. E., Weinberger, A. J., & Wyatt, M. C. 2007, in *Protostars and Planets V*, ed. B. Reipurth, D. Jewitt, & K. Keil, 573
- Mizuno, A., Hayakawa, T., Yamaguchi, N., et al. 1998, *ApJ*, 507, L83
- Mizuno, A., Yamaguchi, R., Tachihara, K., et al. 2001, *PASJ*, 53, 1071
- Moerchen, M. M., Telesco, C. M., & Packham, C. 2010, *ApJ*, 723, 1418
- Montesinos, B., Eiroa, C., Mora, A., & Merín, B., 2009, *A&A*, 495, 901
- Moór, A., Abraham, P., Juhász, A., et al. 2011, *ApJ*, 740, L7
- Nyman, L.-A., Booth, R. S., Carlstrom, U., et al. 1992, *A&AS*, 93, 121
- Öberg, K. I., Qi, C., Fogel, J. K. J., et al. 2011, *ApJ*, 734, 98
- Ohashi, N. 2008, *Ap&SS*, 313, 101
- Onishi, T., Kawamura, A., Abe, R., et al. 1999, *PASJ*, 51, 871
- Ortiz, R., Lorenz-Martins, S., Maciel, W. J., & Rangel, E. M. 2005, *A&A*, 431, 565
- Owen, J. E., Clarke, C. J., & Ercolano, B. 2012, *MNRAS*, 422, 1880
- Panić, O., & Hogerheijde, M. R. 2009, *A&A*, 508, 707

- Panić, O., van Dishoeck, E. F., Hogerheijde, M. R., et al. 2010, *A&A*, 519, A110
- Pascucci, I., Gorti, U., Hollenbach, D., et al. 2006, *ApJ*, 651, 1177
- Pavlyuchenkov, Y., Semenov, D., Henning, T., et al. 2007, *ApJ*, 669, 1262
- Pinte, C., Ménard, F., Duchêne, G., & Bastien, P. 2006, *A&A*, 459, 797
- Pollack, J. B., Hubickyj, O., Bodenheimer, P., et al. 1996, *Icarus*, 124, 62
- Qi, C., D’Alessio, P., Öberg, K. I., et al. 2011, *ApJ*, 740, 84
- Redfield, S., Kessler-Silacci, J. E., & Cieza, L. A. 2007, *ApJ*, 661, 944
- Rhee, J. H., Song, I., Zuckerman, B., & McElwain, M. 2007a, *ApJ*, 660, 1556
- Rhee, J. H., Song, I., & Zuckerman, B. 2007b, *ApJ*, 671, 616
- Rieke, G. H., Su, K. Y. L., Stansberry, J. A., et al. 2005, *ApJ*, 620, 1010
- Sandell, G., Weintraub, D. A., & Hamidouche, M. 2011, *ApJ*, 727, 26
- Schütz, O., Bönhardt, H., Pantin, E., et al. 2004, *A&A*, 424, 613
- Schütz, O., Meeus, G., Carmona, A., Juhász, A., & Sterzik, M. F. 2011, *A&A*, 533, A54
- Shimoikura, T., & Dobashi, K. 2011, *ApJ*, 731, 23
- Silverstone, M. D. 2000, Ph.D. Thesis, University of California
- Siringo, G., Kreysa, E., Kovács, A., et al. 2009, *A&A*, 497, 945
- Straizys, V., Černis, K., & Bartasiute, S. 1996, *Baltic Astronomy*, 5, 125
- Sylvester, R. J., & Mannings, V. 2000, *MNRAS*, 313, 73
- Tachihara, K., Mizuno, A., & Fukui, Y. 2000, *ApJ*, 528, 817

- Takeuchi, T., & Artymowicz, P. 2001, *ApJ*, 557, 990
- Tatulli, E., Isella, A., Natta, A., et al. 2007, *A&A*, 464, 55
- Thé, P. S., de Winter, D., & Perez, M. R. 1994, *A&AS*, 104, 315
- Thi, W. F., van Dishoeck, E. F., Blake, G. A., et al. 2001, *ApJ*, 561, 1074
- van der Plas, G., van den Ancker, M. E., Fedele, D., et al. 2008, *A&A*, 485, 487
- van Kempen, T. A., van Dishoeck, E. F., Brinch, C., & Hogerheijde, M. R. 2007, *A&A*, 461, 983
- van Leeuwen, F. 2007, *A&A*, 474, 653
- Verhoeff, A. P., Min, M., Acke, B., et al. 2010, *A&A*, 516, A48
- Vieira, S. L. A., Corradi, W. J. B., Alencar, S. H. P., et al. 2003, *AJ*, 126, 2971
- Wade, G. A., Bagnulo, S., Drouin, D., Landstreet, J. D., & Monin, D. 2007, *MNRAS*, 376, 1145
- Walker, H. J., & Wolstencroft, R. D. 1988, *PASP*, 100, 1509
- Walsh, C., Millar, T. J., & Nomura, H. 2010, *ApJ*, 722, 1607
- Weidenschilling, S. J. 1977, *MNRAS*, 180, 57
- Williams, J. P., & Cieza, L. A. 2011, *ARA&A*, 49, 67
- Wyatt, M. C., Greaves, J. S., Dent, W. R. F., & Coulson, I. M. 2005, *ApJ*, 620, 492
- Wyatt, M. C. 2008, *ARA&A*, 46, 339
- Wyatt, M. C., Smith, R., Su, K. Y. L., et al. 2007, *ApJ*, 663, 365

- Woitke, P., Kamp, I., & Thi, W.-F. 2009, *A&A*, 501, 383
- Yamamura, I., et al., 2011, AKARI/FIS All-Sky Survey Bright Source Catalogue Version 1.0 Release Note, <http://www.ir.isas.jaxa.jp/AKARI/Observation/PSC/Public/>
- Yi, S., Demarque, P., Kim, Y.-Ch., et al., 2001, *ApJS*, 136, 417
- Zagorovsky, K., Brandeker, A., & Wu, Y. 2010, *ApJ*, 720, 923
- Zhang, X., Lee, Y., Bolatto, A., & Stark, A. A. 2001, *ApJ*, 553, 274
- Zuckerman, B., Forveille, T., & Kastner, J. H. 1995, *Nature*, 373, 494
- Zuckerman, B. 2001, *ARA&A*, 39, 549

Table 1. Target Sample

Star	Ra (J2000)	Dec (J2000)	Sp. Type	Distance (pc)	L_{IR}/L_*	CO intensity ^f (K km s ⁻¹)	Disk group	Reference	
1	HD 105	00:05:52.5	-41:45:11.0	G0V	40	5.9×10^{-4}	$< 0.02^e$	Debris Disk	Hillenbrand et al. (2008)
2	HR 10	00:07:18.2	-17:23:13.1	A2IV/V	160	6.6×10^{-7}	$< 0.09^c$	Debris Disk	Possible bogus IRAS identification (Fajardo-Acosta et al. 1998a).
3	HD 377	00:08:25.7	+06:37:00.4	G2V	40	5.8×10^{-4}	$< 0.09^a$	Debris Disk	Hillenbrand et al. (2008)
4	HD 3003	00:32:43.9	-63:01:53.4	A0V	46	1.4×10^{-4}	$< 0.11^a$	Debris Disk	Rhee et al. (2007a)
5	HD 12039	01:57:48.9	-21:54:05.3	G4V	42	2.1×10^{-4}	$< 0.02^e$	Debris Disk	Rhee et al. (2007a)
6	HD 17848	02:49:01.4	-62:48:23.4	A2V	50	3.9×10^{-5}	$< 0.14^d$	Debris Disk	Sylvester & Mannings (2000)
7	HD 21563	03:24:02.3	-69:37:28.5	A4V	182	9.7×10^{-3}	$< 0.11^d$	Debris Disk	Sylvester & Mannings (2000)
8	HD 28001	04:22:05.9	-56:58:59.5	A4V	-	5.0×10^{-3}	$< 0.11^d$	Debris Disk	Sylvester & Mannings (2000)
9	HD 32297	05:02:27.4	+07:27:39.6	A0	112	5.4×10^{-3}	$< 0.05^c$	Debris Disk	Rhee et al. (2007a); L_{IR}/L_* from Meeus et al. (2012)
10	HD 36917	05:34:46.9	-05:34:14.5	A0V	460(5)	1.0×10^{-1}	1.1 ± 0.5^e	HAeBe disk	Malfait et al. (1998)
11	HD 37411	05:38:14.5	-05:25:13.2	B9 V	510(13)	3.9×10^{-1}	0.5 ± 0.25^e	HAeBe disk	Malfait et al. (1998)
12	HD 37258	05:36:59.2	-06:09:16.3	A2V	510(6)	3.7×10^{-1}	4.8 ± 1.2^b	HAeBe disk	Malfait et al. (1998)
13	HD 37389	05:38:08.0	-01:45:07.8	A0	210(7)	1.2×10^{-2}	3.1 ± 0.5^b	HAeBe disk	Coulson et al. (1998)
14	HD 38087	05:43:00.5	-02:18:45.3	B5 V	199	1.9×10^{-2}	4.5 ± 1.1^e	HAeBe disk	Malfait et al. (1998)
15	HD 39014	05:44:46.3	-65:44:07.9	A7 V	44	5.7×10^{-5}	$< 0.02^e$	HAeBe disk	Malfait et al. (1998)
16	HD 250550	06:01:59.9	+16:30:56.7	B9	606(8)	1.4	7.9 ± 1.7^c	HAeBe disk	de Winter et al. (2001)
17	HD 61005	07:35:47.4	-32:12:14.0	G8V	34	6.8×10^{-4}	$< 0.02^c$	Debris Disk	Hillenbrand et al. (2008)
18	HD 85567	09:50:28.5	-60:58:02.9	B2	770(9)	3.3×10^{-1}	1.4 ± 0.4^e	HAeBe disk	Malfait et al. (1998)
19	HD 95881	11:01:57.6	-71:30:48.3	A1/2III	118(1)	6.2×10^{-2}	$< 0.02^e$	HAeBe disk	Malfait et al. (1998)
20	HD 97048	11:08:03.3	-77:39:17.4	A0pshe	175	3.9×10^{-1}	1.4 ± 0.4^c	HAeBe disk	de Winter et al. (2001); L_{IR}/L_* from Meeus et al. (2012)
21	Hen3-600	11:10:27.8	-37:31:52.0	M4Ve	42(2)	6.6×10^{-2}	$< 0.02^c$	T Tauri Disk	Rhee et al. (2007b)
22	HD 98922	11:22:31.6	-53:22:11.4	A2 IIIe	115	6.5×10^{-1}	0.11 ± 0.03^e	HAeBe disk	Malfait et al. (1998)

Table 1—Continued

Star	Ra (J2000)	Dec (J2000)	Sp. Type	Distance (pc)	L_{IR}/L_*	CO intensity ^f (K km s ⁻¹)	Disk group	Reference	
23	HD 100453	11:33:05.5	-54:19:28.5	A9Ve	111	6.2×10^{-1}	$< 0.07^b$	HAeBe disk	Malfait et al. (1998); L_{IR}/L_* from Meeus et al. (2012)
24	HD 100546	11:33:25.4	-70:11:41.2	B9Vne	103	5.6×10^{-1}	2.5 ± 0.3^c	HAeBe disk	Malfait et al. (1998); L_{IR}/L_* from Meeus et al. (2012)
25	HD 101412	11:39:44.4	-60:10:27.7	B9.5V	160(12)	1.5×10^{-1}	$< 0.07^c$	HAeBe disk	de Winter et al. (2001)
26	HD 104237	12:00:05.0	-78:11:34.5	A4/5V	116	3.2×10^{-1}	0.11 ± 0.04^e	HAeBe disk	Malfait et al. (1998); L_{IR}/L_* from Meeus et al. (2012)
27	HD 109573A	12:36:01.0	-39:52:10.2	A0	67	5.0×10^{-3}	$< 0.05^b$	Debris Disk	Rhee et al. (2007a)
28	HD 110058	12:39:46.1	-49:11:55.5	A0V	100	2.5×10^{-3}	$< 0.05^c$	Debris Disk	Rhee et al. (2007a)
29	HD 113766	13:06:35.8	-46:02:02.0	F4V	131	2.1×10^{-2}	$< 0.05^c$	Debris Disk	Rhee et al. (2007b)
30	PDS 66	13:22:07.5	-69:38:12.1	K1Ve	86(2)	1.3×10^{-1}	$< 0.09^a$	T Tauri Disk	Hillenbrand et al. (2008)
31	HD 124237	14:14:33.6	-61:47:56.3	B5 V	452	1.6×10^{-1}	$< 0.09^e$	HAeBe disk	Malfait et al. (1998)
32	HD 132947	15:04:56.0	-63:07:52.6	A0	-	2.3×10^{-2}	0.26 ± 0.05^b	HAeBe disk	Malfait et al. (1998)
33	HD 140863	15:48:49.4	-57:37:55.3	A0 III	-	5.2×10^{-1}	$< 0.02^e$	HAeBe disk	Malfait et al. (1998)
34	HD 142527	15:56:41.8	-42:19:23.2	F6IIIe	198	9.8×10^{-1}	1.7 ± 0.7^b	HAeBe disk	Malfait et al. (1998); L_{IR}/L_* from Meeus et al. (2012)
35	ScoPMS31	16:06:21.9	-19:28:44.5	M0	145(10)	1.2×10^{-1}	$< 0.02^e$	T Tauri disk	Dahm & Carpenter (2009)
36	HD 144668	16:08:34.2	-39:06:18.3	A7IVe	207	5.1×10^{-1}	7.2 ± 2.0^b	HAeBe disk	Malfait et al. (1998); L_{IR}/L_* from Meeus et al. (2012)
37	HD 149914	16:38:28.6	-18:13:13.7	B9.5IV	165	1.3×10^{-3}	1.1 ± 0.4^b	HAeBe disk	Malfait et al. (1998)
38	HD 155448	17:12:58.7	-32:14:33.5	B 9	606	6.0×10^{-2}	0.11 ± 0.02^e	HAeBe disk	Malfait et al. (1998)
39	KK Oph	17:10:08.0	-27:15:18.2	A8Ve	160(4)	2.0	0.6 ± 0.2^a	HAeBe disk	de Winter et al. (2001); L_{IR}/L_* from Meeus et al. (2012)
40	HD 158352	17:28:49.6	+00:19:50.2	A8Vp	63	1.6×10^{-4}	$< 0.6^c$	Debris Disk	Rhee et al. (2007a); L_{IR}/L_* from Meeus et al. (2012)
41	HD 158643	17:31:24.9	-23:57:45.5	A0V	131	3.8×10^{-2}	$< 0.09^c$	HAeBe disk	Malfait et al. (1998)
42	sao185668	17:43:55.6	-22:05:44.7	B3	700(7)	1.1×10^{-1}	$< 0.02^e$	HAeBe disk	Malfait et al. (1998)
43	HR 6629	17:47:53.5	+02:42:26.2	A0V	29	4.0×10^{-5}	$< 0.09^b$	Debris Disk	Fajardo-Acosta et al. (1998b)
44	HR 6723	18:01:45.1	+01:18:18.2	A2Vn	81	5.0×10^{-5}	$< 0.4^c$	Debris Disk	Rieke et al. (2005)

Table 1—Continued

Star	Ra (J2000)	Dec (J2000)	Sp. Type	Distance (pc)	L_{IR}/L_*	CO intensity ^f (K km s ⁻¹)	Disk group	Reference
45 VV Ser	18:28:47.8	+00:08:39.9	-	260(3)	9.1	0.47 ± 0.08^c	HAeBe disk	de Winter et al. (2001)
46 RX J1842.9-353	18:42:57.9	-35:32:42.7	K2	130	8.0×10^{-2}	0.14 ± 0.03^a	T Tauri Disk	Hillenbrand et al. (2008)
47 HD 172555	18:45:26.9	-64:52:16.5	A7V	29	8.1×10^{-4}	$< 0.02^e$	Debris Disk	Rhee et al. (2007a)
48 RX J1852.3-370	18:52:17.2	-37:00:11.9	K7V	130	1.8×10^{-1}	$< 0.09^a$	T Tauri Disk	Hillenbrand et al. (2008)
49 HD 181327	19:22:58.9	-54:32:16.9	F6V	50	8.7×10^{-4}	$< 0.02^e$	Debris Disk	Rhee et al. (2007a)
50 HD 178253	19:09:28.3	-37:54:16.1	A2V	39	3.9×10^{-5}	0.57 ± 0.1^e	Debris Disk	Sylvester & Mannings (2000)
51 HD 181296	19:22:51.2	-54:25:26.1	A0V	47	2.4×10^{-4}	$< 0.18^d$	Debris Disk	Rhee et al. (2007a)
52 HD 184800	19:38:40.8	-51:00:18.5	A8/9V	-	1.3×10^{-1}	$< 0.09^b$	Debris Disk	Sylvester & Mannings (2000)

Spectral types are from Michigan Spectral Catalogue and distances are derived from parallax measures listed in the *Hipparcos* catalogue; other references for distance are: 1) Acke & van den Ancker (2004), 2) Rhee et al. (2007b), 3) Straizys et al. (1996), 4) Sandell et al. (2011) - 5) Distance to the Ori OB1 association e.g. Hamaguchi et al. (2005), (6) Liu et al. (2011), 7) Coulson et al. (1998), 8) Brittain et al. (2007), 9) Vieira et al. (2003), 10) Distance to the Upper Scorpius OB association e.g. de Zeeuw et al. (1999), 11) Kun et al. (2000), 12) Acke et al. (2005), 13) Wade et al. (2007). The four detections free of CO emission from extended gas associated with ambient molecular cloud material are marked in bold faces.

^aASTE, June 2008

^bAPEX, June 2008

^cAPEX, July 2009

^dAPEX, December 2009

^eASTE, July 2010

^fIntensity units are in antenna temperatures (T_A^*). Upper limits were computed over 10 km s⁻¹ velocity interval.

Table 2: HD 104237 photometric data

Wavelength	Flux	Flux Error	Reference	Reference
(μm)	($\text{erg}/\text{cm}^{-2}/\text{s}/\text{\AA}$)	($\text{erg}/\text{cm}^{-2}/\text{s}/\text{\AA}$)	Filter	
0.345	6.8022E-12	6.8022E-13	u	Hauck & Mermilliod (1998)
0.347	6.9823E-12	6.9823E-13	U	Malfait et al. (1998)
0.411	1.3423E-11	1.3423E-12	v	Hauck & Mermilliod (1998)
0.425	1.2706E-11	1.2706E-12	B	Malfait et al. (1998)
0.440	1.2443E-11	1.6045E-13	B	Høg et al. (2000)
0.467	1.2078E-11	1.2078E-12	b	Hauck & Mermilliod (1998)
0.548	8.5312E-12	8.5312E-13	y	Hauck & Mermilliod (1998)
0.550	8.7983E-12	8.7983E-13	V	Malfait et al. (1998)
0.550	8.3176E-12	7.6609E-14	V	Høg et al. (2000)
0.640	5.1643E-12	5.1643E-13	R	Cutri et al. (2003)
1.215	1.6590E-12	1.6590E-13	J	Malfait et al. (1998)
1.235	1.4818E-12	3.1391E-14	J	Cutri et al. (2003)
1.654	1.0114E-12	1.0114E-13	H	Malfait et al. (1998)
1.662	8.8605E-13	4.8173E-14	H	Cutri et al. (2003)
2.159	6.2851E-13	1.0420E-14	K_s	Cutri et al. (2003)
2.179	7.0558E-13	7.0558E-14	K	Malfait et al. (1998)
3.547	3.9628E-13	3.9628E-14	L	Malfait et al. (1998)
4.769	1.9592E-13	1.9592E-14	M	Malfait et al. (1998)
12.000	3.4073E-14	3.4073E-15	12 μm	Beichman et al. (1988)
25.000	7.8464E-15	7.8464E-16	25 μm	Beichman et al. (1988)
60.000	7.0254E-16	7.0254E-17	60 μm	Beichman et al. (1988)

Note. — Table 2 is published in its entirety in the electronic edition of the Journal. A portion is shown here for guidance regarding its form and content.

Table 3: HD 104237 disk model

Physical parameter	Value	Reference
Stellar properties		
Spectral type 1	A4V	Tatulli et al. (2007)
Spectral type 2	K3V	Tatulli et al. (2007)
Primary star Mass: M_1 (M_\odot)	2.2	Garcia et al. (2013)
Secondary star Mass : M_2 (M_\odot)	1.4	Garcia et al. (2013)
Effective temperature: T_1 (K)	8000	Tatulli et al. (2007)
Effective temperature: T_2 (K)	4750	Tatulli et al. (2007)
Stellar Luminosity: L_1 (L_\odot)	30	Tatulli et al. (2007)
Stellar Luminosity: L_2 (L_\odot)	3	Tatulli et al. (2007)
Distance: d (pc)	115	Tatulli et al. (2007)
Disk structure		
Disk total mass: M_D (M_\odot)	$100 \times M_d$	this work
Disk dust mass M_d (M_\odot)	4×10^{-4}	this work
Inner Rim: R_{in} (AU)	0.45	Tatulli et al. (2007)
Characteristic radius R_C (AU)	90	this work
Characteristic height h_C (AU)	6	this work
Surface density exponent: γ	0.8	this work
Flaring exponent: ψ	0.0	this work
Inclination angle: i (deg)	31	this work
Systemic Velocity: V_{lsr} (km/s)	4.2	this work

Table 4: HD 98922 photometric data

Wavelength	Flux	Flux Error	Reference	Reference
(μm)	($\text{erg}/\text{cm}^{-2}/\text{s}/\text{\AA}$)	($\text{erg}/\text{cm}^{-2}/\text{s}/\text{\AA}$)	Filter	
0.347	6.7298E-12	6.7298E-13	U	Malfait et al. (1998)
0.425	1.3305E-11	1.3305E-12	B	Malfait et al. (1998)
0.440	1.2489E-11	1.2489E-12	B	Høg et al. (2000)
0.550	7.3858E-12	7.3858E-13	V	Malfait et al. (1998)
0.550	7.5370E-12	7.5370E-13	V	Høg et al. (2000)
0.548	7.1682E-12	3.3011E-13	y	Hauck & Mermilliod (1998)
1.215	1.1478E-12	1.1478E-13	J	Malfait et al. (1998)
1.235	1.2427E-12	2.2893E-14	J	Cutri et al. (2003)
1.654	8.2592E-13	8.2592E-14	H	Malfait et al. (1998)
1.662	9.0252E-13	2.4109E-14	H	Cutri et al. (2003)
2.179	7.1211E-13	7.1211E-14	K	Malfait et al. (1998)
2.159	8.3236E-13	2.7604E-14	K _s	Cutri et al. (2003)
3.547	4.9889E-13	4.9889E-14	K	Malfait et al. (1998)
4.769	2.6797E-13	2.6797E-14	M	Malfait et al. (1998)
12.000	6.3403E-14	6.3403E-15	12 μm	Beichman et al. (1988)
25.000	9.2532E-15	9.2532E-16	25 μm	Beichman et al. (1988)
60.000	3.5550E-16	3.5550E-17	60 μm	Beichman et al. (1988)
65.000	2.3016e-16	1.6985e-17	65 μm	Yamamura et al. (2011)
70.000	2.1909e-16	1.0954e-17	70 μm	PACS (This work)
90.000	9.5968e-17	5.2938e-18	90 μm	Yamamura et al. (2011)
140.000	1.7314e-17	7.9813e-18	140 μm	Yamamura et al. (2011)
160.000	1.0270e-17	5.1351e-19	160 μm	PACS (This work)

Table 5: HD 98922 disk model

Physical parameter	Value	Reference
Stellar properties		
Spectral type	A2 III	This work
Primary star Mass: M (M_{\odot})	5.0	This work
Effective temperature: T (K)	9000	This work
Stellar Radius: R (R_{\odot})	9.0	This work
Distance: d (pc)	$d = 507$	This work
Disk structure		
Disk total mass: M_D (M_{\odot})	$100 \times M_d$	this work
Disk dust mass M_d (M_{\odot})	2×10^{-5}	this work
Inner Rim: R_{in} (AU)	1.5	this work
Characteristic radius R_C (AU)	320	this work
Characteristic height h_C (AU)	0.15	this work
Surface density exponent: γ	1.0	this work
Flaring exponent: ψ	0.0	this work
Inclination angle: i (deg)	20	this work
Systemic Velocity: V_{lsr}	-8	this work

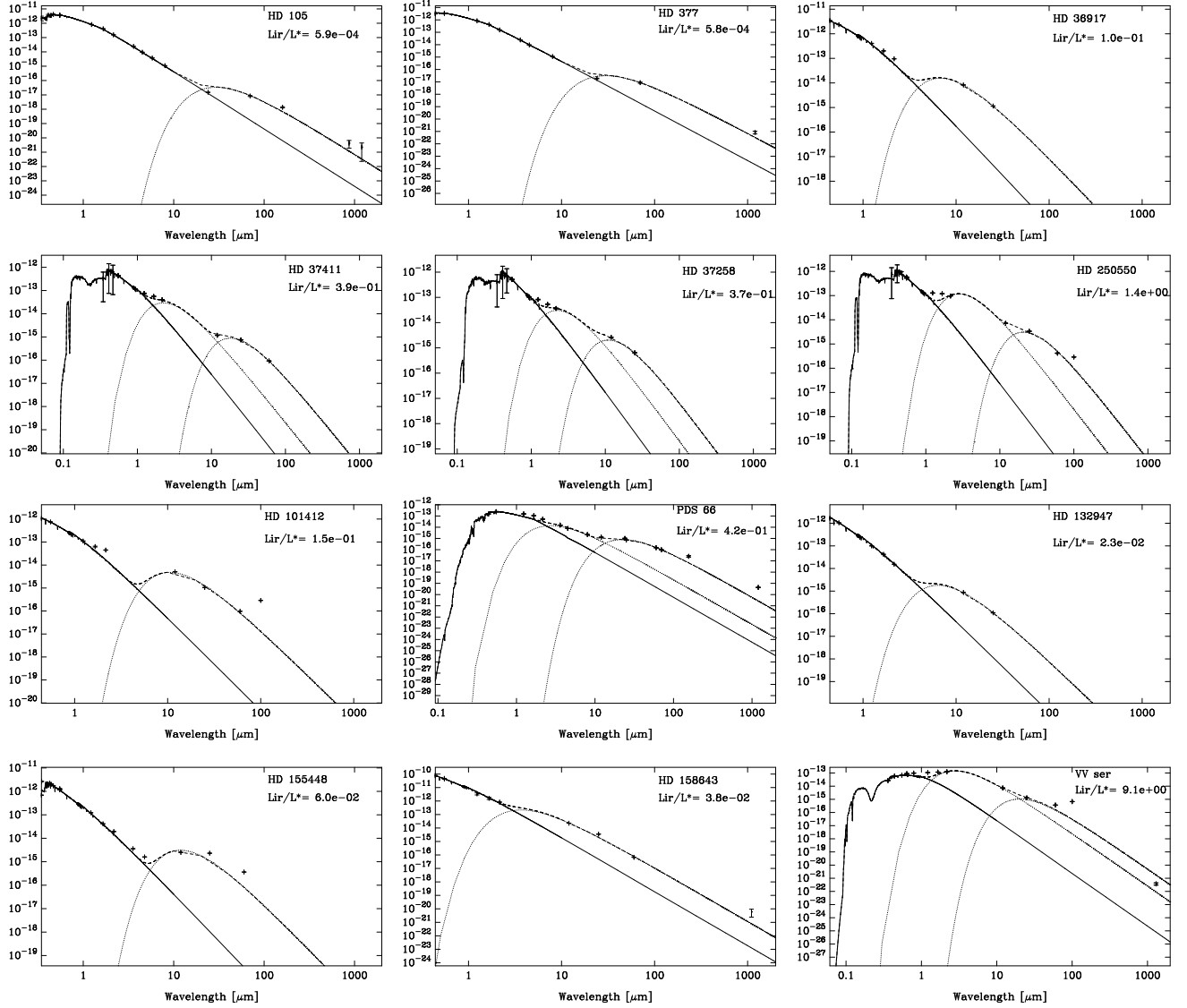


Fig. 1.— Example of our blackbody fit to the available photometry in order to derive L_{IR}/L_* values for stars for which infrared excess were not found in the literature. Units in the vertical axis are in $\text{erg}/\text{cm}^{-2}/\text{s}$.

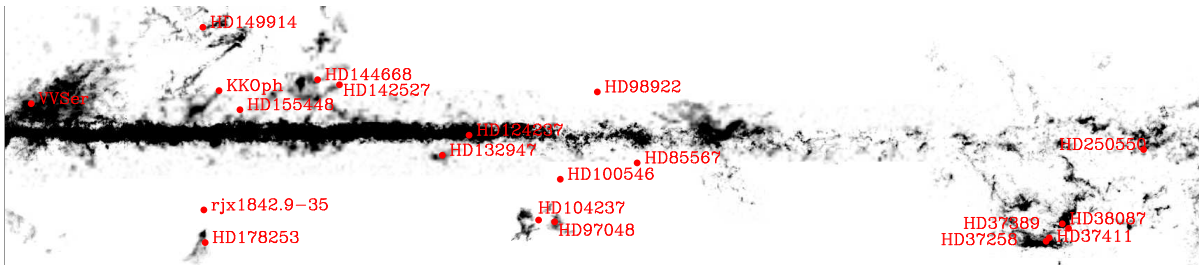


Fig. 2.— Location of southern HAeBe with CO(3-2) detections shown against known molecular clouds CO maps (from Milky Way CO Dame et al. (2001)).

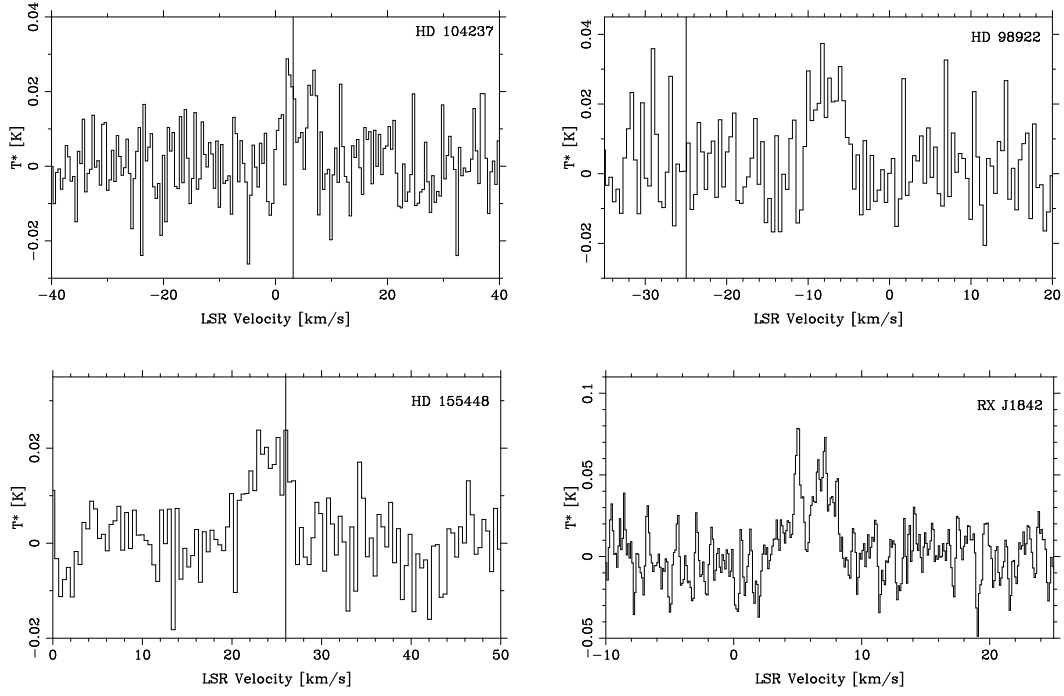


Fig. 3.— Aste spectra for the four new CO disk detections. When available, the stellar velocity has been plotted with a vertical line (in V_{lsr}). Intensity units are in antenna temperature (T_A^*).

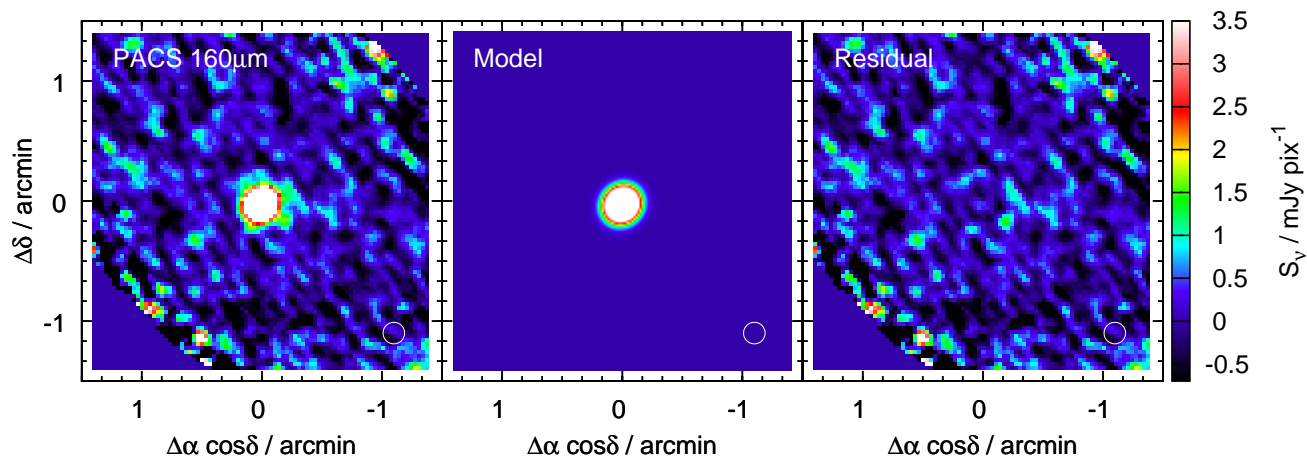


Fig. 4.— *Left:* *Herschel*/PACS 160 μm map around HD 98922 (from archive). *Center:* Gaussian source model used for photometric extraction (total $F_\nu = 878 \pm 44$ mJy, FWHM = $11.0 \times 11.9''$). *Right:* residual map after source subtraction. FWHM beam circles of $10.7''$ diameter are shown.

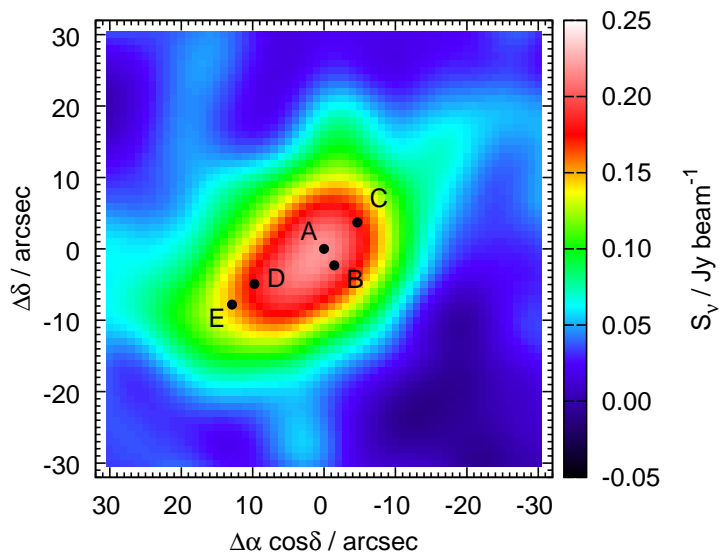


Fig. 5.— LABOCA map of HD 104237 smoothed with half-beam Gaussian (FWHM = $9.3''$), with stellar component positions plotted (component A corresponds to HD 104237).

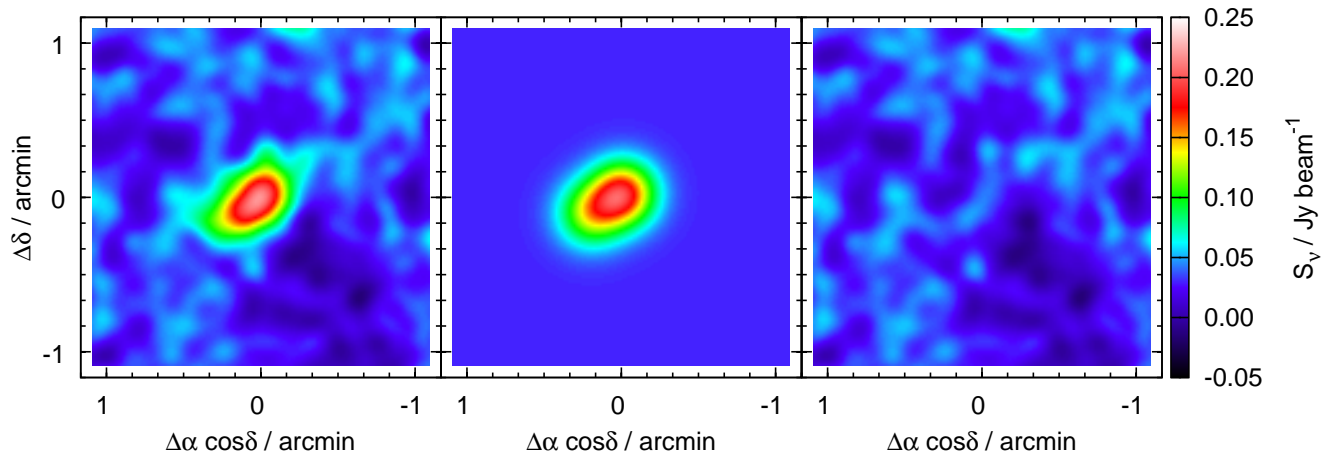


Fig. 6.— *Left*: LABOCA map; *center*: fitted model of 2 effective beam-sized Gaussians (FWHM = 18.6) with separation of A and E components; *Right*: maps with model subtracted.

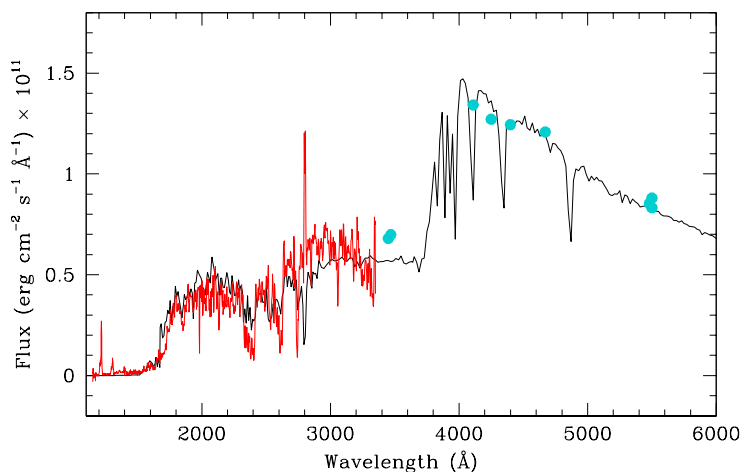


Fig. 7.— HD 104237 spectral type fit to the *IUE* (red line) and optical data (blue dots). The synthetic spectra (black line) corresponds to the sum of two Kurucz models ($T_1 = 8000$, $\log(g_1) = 4.0$ and $T_2 = 4750$, $\log(g_2) = 4.5$); Kurucz 1993), where the second model was scaled such as the integral of the first one divided by the integral of the second one is 10. The combined model has been computed adding up these two files. The combined model has been normalized to the flux at V with no reddening and with $E(B-V) = 0.05$. The best fit does not seem to require any reddening.

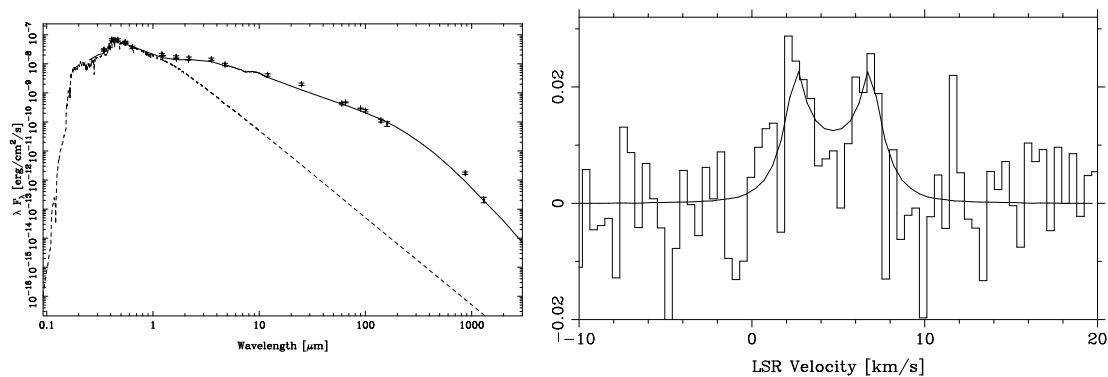


Fig. 8.— *Left*: Observed SED of HD 104237 (black points with error bars) plotted against the MCFOST disk model that fits the optical to sub-mm data (solid line) . The full photometric data is available in the online version of the article. *Right*: MCFOST CO model of HD 104237 (solid line) fits well the ASTE sub- mm data. Intensity units are in antenna temperature (T_A^*).

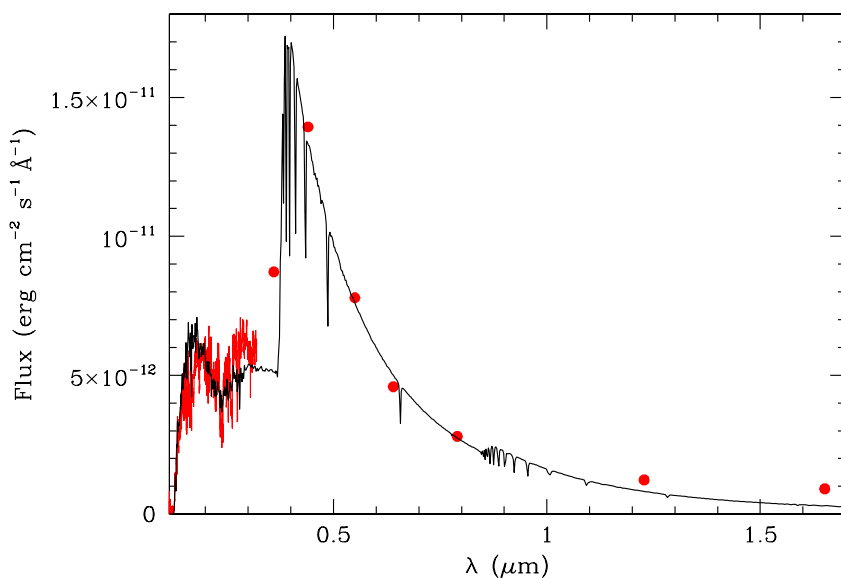


Fig. 9.— The observed spectral energy distribution of HD 98922 (red line and dots) and the fit of a low-resolution Kurucz model (black) computed with $T_{\text{eff}} = 9000$ K, $\log g_* = 3.0$, $[\text{Fe}/\text{H}] = -0.5$ reddened with $E(B - V) = 0.07$ ($R_V = 3.1$) normalized to the flux at I . The ultraviolet spectrum is a composite of the IUE spectra SWP 18553, SWP50065, SWP50083, LWR14624, LWP30007, LWP30026 that were retrieved from the archive at the CAB Science Data Centre (<http://sdc.cab.inta-csic.es/ines/>).

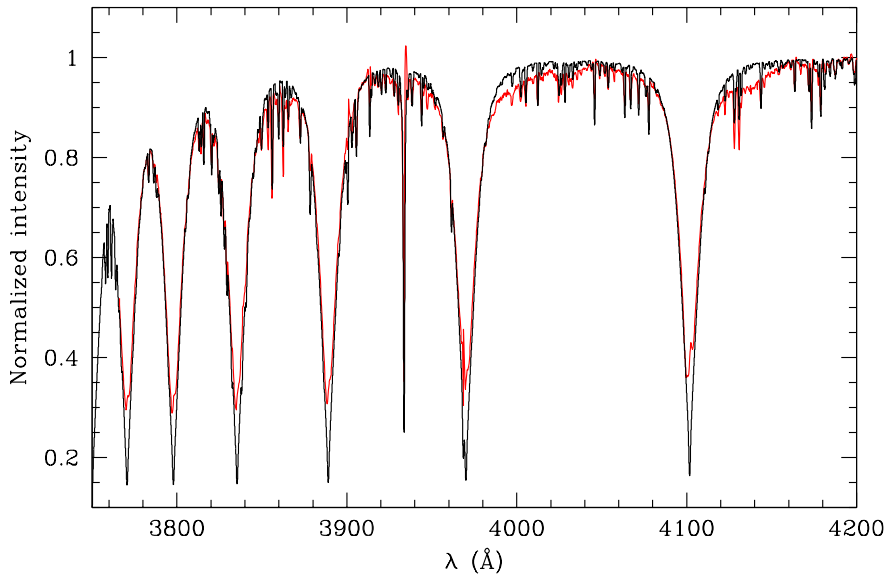


Fig. 10.— The region 3750–4200 Å of the spectrum of HD 98922 obtained with UVES/VLT (red) and the synthetic spectrum (black) computed with the Kurucz ATLAS9 and SYNTHE codes for $T_{\text{eff}}=9000$ K, $\log g_*=3.0$, $[\text{Fe}/\text{H}]=-0.5$ (see text for details).

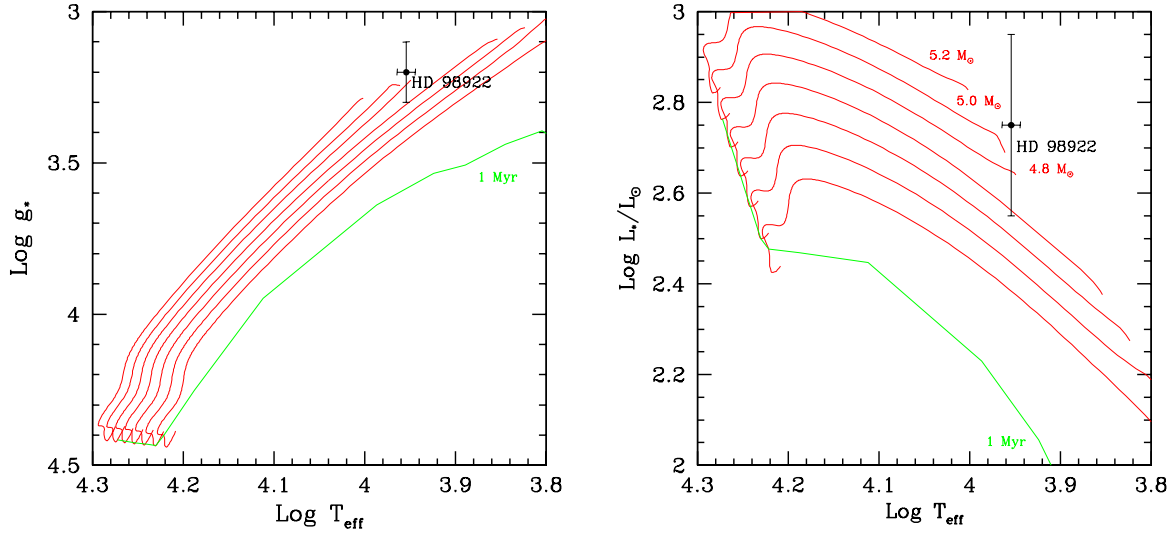


Fig. 11.— $\log g_*$ – $\log T_{\text{eff}}$ and $\log L_*/L_{\odot}$ – $\log T_{\text{eff}}$ HR diagrams showing evolutionary tracks for 4.0, 4.2, 4.4, 4.6, 4.8, 5.0 and 5.2 M_{\odot} and the 1-Myr isochrone from the Yonsei-Yale collection for $Z = 0.007$. The position of a star with $T_{\text{eff}} = 9000$ K and $\log g_* = 3.2$ in the diagram on the left is translated in a one-to-one correspondence to the HR diagram on the right to obtain the luminosity. The value of L_* , and the estimate of the dereddened observed photospheric flux, F_{phot} allows us to calculate the distance to the star (see text for details). The position of star with respect to the isochrone indicates that the star is younger than 1 Myr.

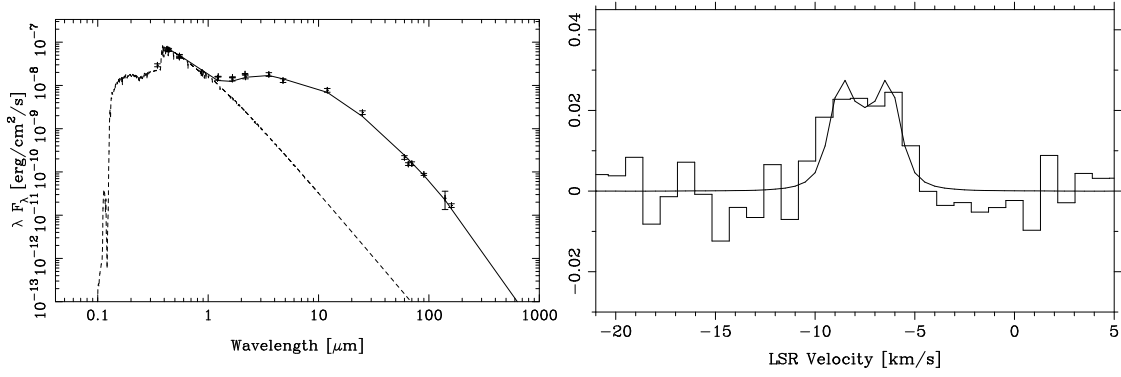


Fig. 12.— *Left:* Observed SED of HD 98922 (black points with error bars) plotted against the MCFOST disk model that fits the optical to far-IR data (solid line). The full photometric data is available in the online version of the article. *Right:* Velocity distribution of the ¹²CO(3-2) line detected from the disk around HD 98922, with the disk model superimposed (solid line). Intensity units are in antenna temperature (T_A^*). The spectrum shown Figure 3 has been smoothed by re-binning into 2 channel averages.

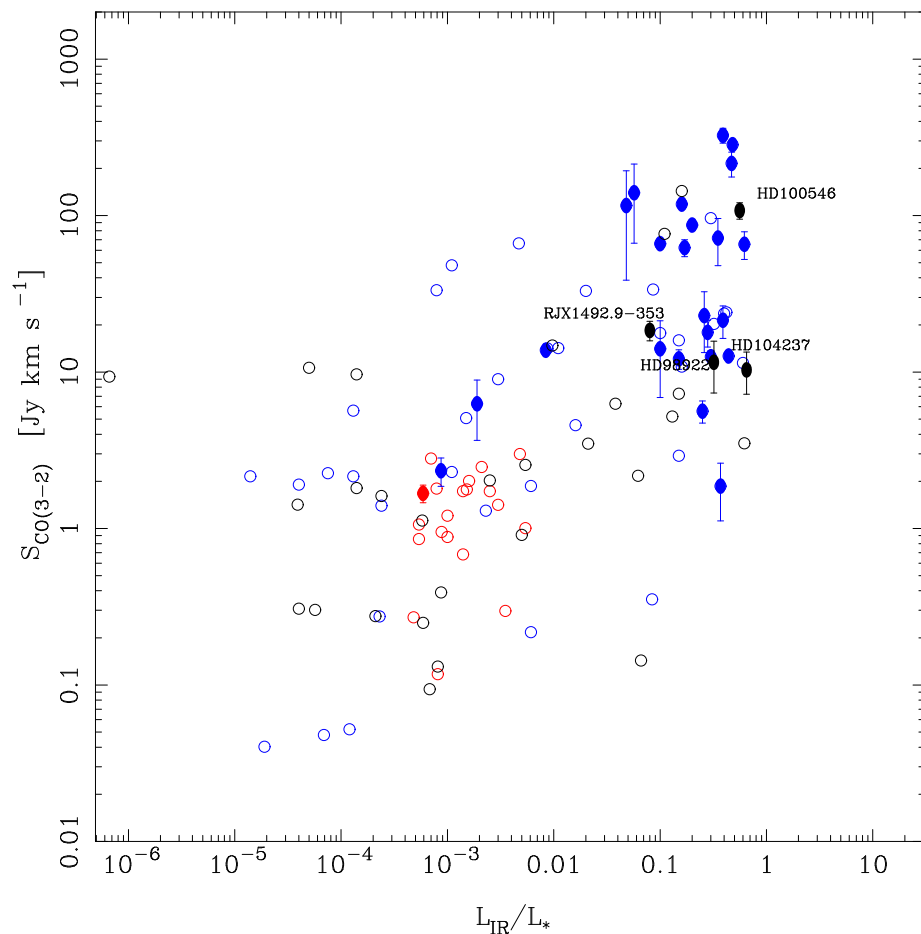


Fig. 13.— Integrated CO intensity or upper limits versus fractional infrared excess for the observed stars (only stars with no cloud contamination, and having both distance estimates and enough SED points for reliable determinations have been included). Black filled circles denote objects with positive detections likely to be associated to circumstellar CO disks, while black open circles are 1-sigma upper limits (computed using 10 km s^{-1} windows, see text). Data from the literature for protoplanetary and debris disk from the CO surveys of Dent et al. (2005) and Moór et al. (2011) are plotted in blue and red respectively.

A. Appendix

A.1. Detections with background/foreground contamination

In this section we present individual sources with CO detections likely to arise from background/foreground contamination.

A.1.1. HD 124237

HD 124237 is located on the galactic plane (Dame et al. 2001), yielding several velocity components of galactic CO detected in our spectra (Figure 14). The line intensities are typical of galactic clouds, and if present, any circumstellar CO emission would be completely dominated by the ambient emission. The intensities of the lines vary significantly when using a different reference position, indication of a strong contamination from ambient CO.

A.1.2. HD 178253

This A2V star, alias α CrA, was originally catalogued as a debris disk type star by Mannings & Barlow (1998) based on data from *IRAS*, and subsequently re-observed with *Spitzer* by Rieke et al. (2005). Mid-infrared imaging using Gemini South failed to detect any significant mid-IR excess towards this star (Moerchen et al. 2010).

HD 178253 is located in the direction of the CrA molecular cloud (Harju et al. 1993), which is clearly seen in the spectrum of the reference (off-) position. HD 178253 has a photospheric radial velocity of $V_{\text{helio}} = -18.4 \pm 2 \text{ km s}^{-1}$ (Barbier-Brossat & Figon 2000), or $V_{\text{lsr}} = -12.3 \text{ km s}^{-1}$. No prominent emission is detected near the tabulated stellar velocity. In addition, as seen in Figure 14, the resulting spectrum changes dramatically when using

a different reference position. Therefore, the CO detection cannot be unambiguously associated to a circumstellar disk.

A.1.3. HD 36917, HD 37411, HD 37389, HD 37258 and HD 38087

HD 36917, HD 37411, HD 37389, HD 37258 and HD 38087 are located in the Orion molecular clouds. The spectra toward these stars is contaminated due to cloud emission in the reference. This is obvious in the case of HD 36917 (Figure 14), where a second observation with a different reference position was acquired. Changing the off-position yielded false absorption features indicative of strong emission in the reference. A similar effect is seen when comparing the two spectra taken towards HD 37411 (Figure 15).

Located in the middle of Orion’s waist, between Alnilam and ζ Ori, HD 37389 is surrounded by the strong background from Orion B. The single-pointing APEX CO(3-2) spectrum gives a narrow line, with a velocity-integrated T_{mb} intensity of 4.2 K km s^{-1} (Figure 16). CO(3-2) probably stems from the diffuse cloud.

Our CHAMP+ follow-up observations (Casassus et al. 2013) show how the diffuse emission is clearly traced in north-western horns of the CHAMP+ footprint (see Appendix A.2 for details).

For HD 37258 and HD 38087 the detected peaks appear too large compared to pure disk emission (Figures 16 and 17). Bogus absorption features due to reference contamination are seen in both spectra. The smaller peaks at 7 km s^{-1} are too narrow to be circumstellar, and also coincide with the $4\text{-}14 \text{ km s}^{-1}$ range of the known clouds in Orion (Dame et al. 2001). CO emission toward these stars is most likely associated to the Orion Molecular Cloud.

A.1.4. HD85567

HD85567 is a B2Ve star first associated to the HAeBe membership by Thé et al. (1994). Its infrared excess of 3.3×10^{-1} is characteristic of young, massive protoplanetary disks. Juhász et al. (2010) reports strong silicate emission detected with the *Spitzer Space Telescope*

We detect a bright single peaked line at 31 km s^{-1} (Figure 17). HD85567 is located close to the galactic plane in the direction of the Carina arm at $(l, b) = (282.6, -5.4)$. CO mappings of the Carina region have not covered the position of HD85567 (Fukui et al. 1999; Zhang et al. 2001; Dawson et al. 2008), therefore no comparison with known cloud velocities is available.

A.1.5. HD 142527

HD 142527 is surrounded by a well-studied circumstellar disk that harbors copious amounts of gas, as detected with the SMA (Ohashi 2008; Öberg et al. 2011). The ASTE spectrum shows clear contamination in the reference position (Figure 18). The emission coincides with the radial velocity of the star.

Our observations towards HD 142527 highlight the difficulties for using CO(3-2) single dish observational techniques to detect unambiguously circumstellar disc emission in environments with high ambient emission. However, our follow up CO(6-5) observations using CHAMP+ in APEX confirm warm CO emission in the position of the star (Casassus et al. 2013), as well as the detection of a double-peaked HCO+(4-3) line. (de Gregorio-Monsalvo et al. 2103). This may suggest that warmer-gas or higher-density gas tracers may indeed be combined with single dish observations to detect circumstellar

gas emission from protoplanetary disks.

Recent ALMA imaging of this gas-rich disk has revealed the existence of CO gas inside the dust cavity, as well as the presence of gap-crossing HCO+ filaments (Casassus et al. 2013).

A.1.6. HD 144668

HD 144668 (V856 Sco, HR5999) is an A7 IVe star which exhibits a large infrared excess ($L_{\text{IR}}/L_* \sim 0.51$), with an age of 2.8 Myr. Strong [O I] 63.2 μm emission towards HD 144668 is detected (Meeus et al. 2012), indicative that its disk still has a large reservoir of orbiting gas.

HD 144668 is located in the direction of the Lupus molecular clouds (Figure 2; Hara et al. 1999). The emission in the CO(3-2) detection spectrum does coincide within errors with the tabulated stellar velocity (Figure 18). But also coincides both in position and velocity with the C¹⁸O core 27 in Hara et al. (1999) ((l,b)=(339.567,933), $V_{\text{lsr}} = 4.12 \text{ km s}^{-1}$). This suggests that the CO emission observed towards the star is dominated by diffuse cloud emission. The detection can be considered as an upper limit to the disk intrinsic CO emission.

A.1.7. HD 97048

HD 97048 (CU Cha) is a well studied A0 star located in the direction of the Chameleon I cloud (Figure 2; Mizuno et al. 1998). (Martin-Zaïdi et al. 2009) detected the Mid-IR H₂ S(1) line at 17 μm , but not the S(2) nor the S(4) at 12 and 8 μm , respectively. Carmona et al. (2011) detect near-IR H₂ 1-0 S(1) using CRIRES on the VLT. Copious

amounts of CO J=19-17, [O I] 145.5 μm and [O I] 63.2 μm emission towards HD 97048 are detected (Meeus et al. 2012). It is also one of the three objects where [C II] 157.7 μm is detected.

The CO spectra is contaminated due to cloud emission in the reference (Figure 19), since the star lies on top of the Cha I molecular cloud. The typical $^{12}\text{CO}(1-0)$ cloud velocities in the Cha I region are in the $V_{\text{lsr}} = 2 - 6 \text{ km s}^{-1}$ range (Mizuno et al. 1998), which concur with the (contaminated) emission we detect.

A.1.8. HD 132947

HD 132947 is located in the fourth galactic quadrant towards the Circinus molecular cloud (Figure 2; Shimoikura & Dobashi 2011). The NANTEN ^{12}CO maps show several velocity components ranging between $V_{\text{lsr}} = -4$ and -6.5 km s^{-1} , in agreement with the contamination seen in the reference position (which produces the false absorption feature seen in the spectrum). A small emission feature is seen near $V_{\text{lsr}} = -22 \text{ km s}^{-1}$, but the lack of information for the stellar velocity hampers any association to possible circumstellar emission (Figure 19).

A.1.9. HD 250550

HD250550 is located towards the Gemini OB1 molecular clouds (Carpenter et al. 1995). Based on existing $^{12}\text{CO}(1-0)$ maps, the velocity of the CO(3-2) emission detected in our spectra (Figure 20) coincides with the known cloud velocity in the direction of HD250550 ($V_{\text{lsr}} = 4.12 \text{ km s}^{-1}$; Carpenter et al. 1995).

A.1.10. HD 149914

$^{12}\text{CO}(3-2)$ emission is detected towards the B9.5 IV star HD 149914, located towards the Ophiucus cloud (Dame et al. 2001). The spectrum shows indications of contamination in the reference position near 0 km s^{-1} (Figure 20). At least four clouds nearby (1-3 degrees) with $V_{\text{lsr}} = 1 - 5 \text{ km s}^{-1}$ are known (Tachihara et al. 2000). The closest core to the line-of-sight of HD 149914 is located at $(l, b) = (359.23, 18.63)$ has a main velocity component $V_{\text{lsr}} = 0.58 \text{ km s}^{-1}$ and width 0.92 km s^{-1} .

A.1.11. KK Oph

KK Oph is a binary system located at the edge of the Pipe Nebula at $(l, b) = (357.06, 7.1)$, close to a C^{18}O core with $V_{\text{lsr}} \sim 3.6 \text{ km s}^{-1}$ (Onishi et al. 1999). Cloud contamination is evident in our CO spectra (Figure 21), although the $[\text{O I}] 63.2 \mu\text{m}$ detection indicates that the KK Oph system harbors a gas rich protoplanetary disk (Meeus et al. 2012).

A.1.12. VV Ser

Our observations show that VV Ser is surrounded by extended $\text{CO}(3-2)$ that contaminates the reference position (Figure 21), with centroid velocity $V_{\text{lsr}} \sim 7 \text{ km s}^{-1}$. Alonso-Albi et al. (2008) reported continuum detection (PdBI), corresponding to a $4 \times 10^{-5} M_{\odot}$ disk, and a $\text{CO}(1-0)$ non-detection (at a 1σ noise limit of 0.3 K in 1 km s^{-1} channels). Liu et al. (2011) detect $\text{CO}(2-1)$ and $\text{CO}(3-2)$ using the KOSMA 3-meter telescope, and suggest that might come from three different velocity components at $5.3, 7.3$ and 9.5 km s^{-1} , respectively. We detect three $^{12}\text{CO}(3-2)$ peaks at these same velocities. VV Ser is located in the direction of the Aquila Rift, which together with the contaminated

spectra indicates that the single-dish observations are dominated by diffuse molecular cloud emission (Dame et al. 2001).

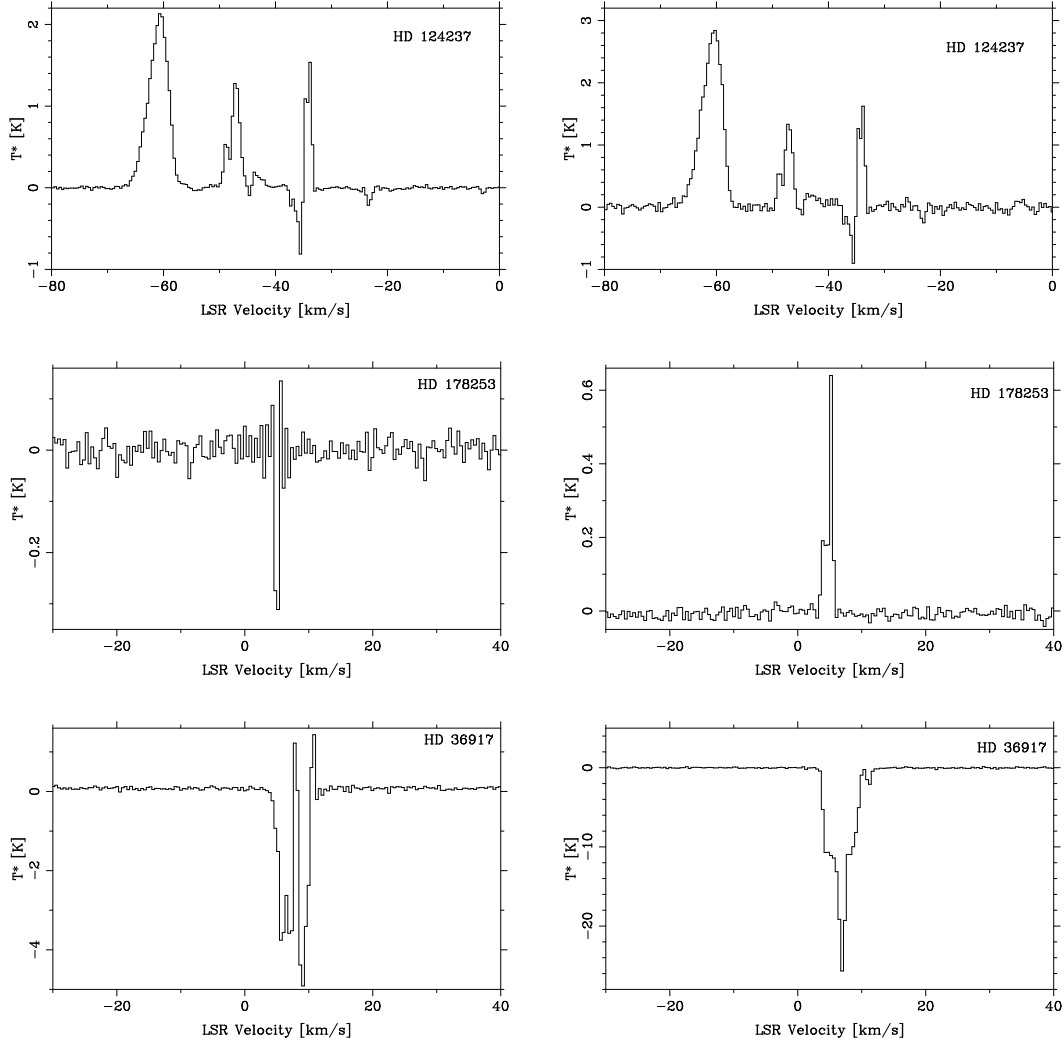


Fig. 14.— Detections with background/foreground contamination in the reference position. The left-hand panels show the spectra obtained using a -180 arcsecond reference position, while the panels on the right present the spectra resulting from a $+180$ arcsecond reference position. When available, the stellar velocity has been plotted with a vertical line (in V_{lsr}). Intensity units are in antenna temperature (T_A^*).

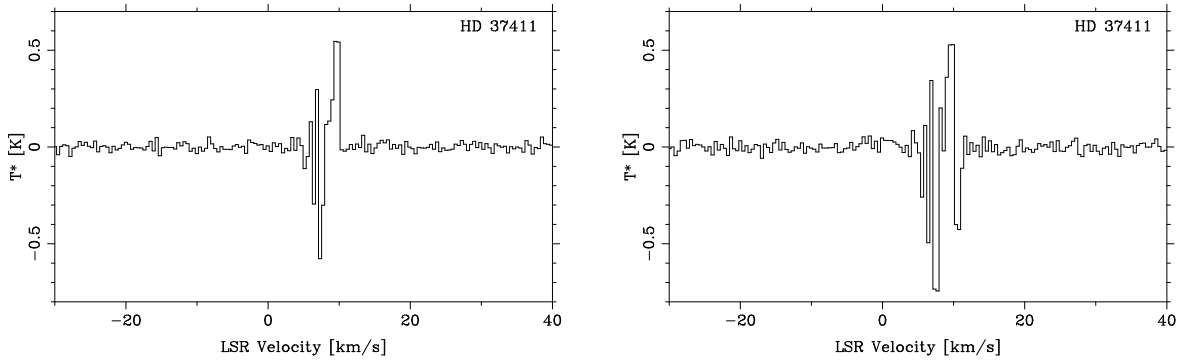


Fig. 15.— Same as Figure 14.

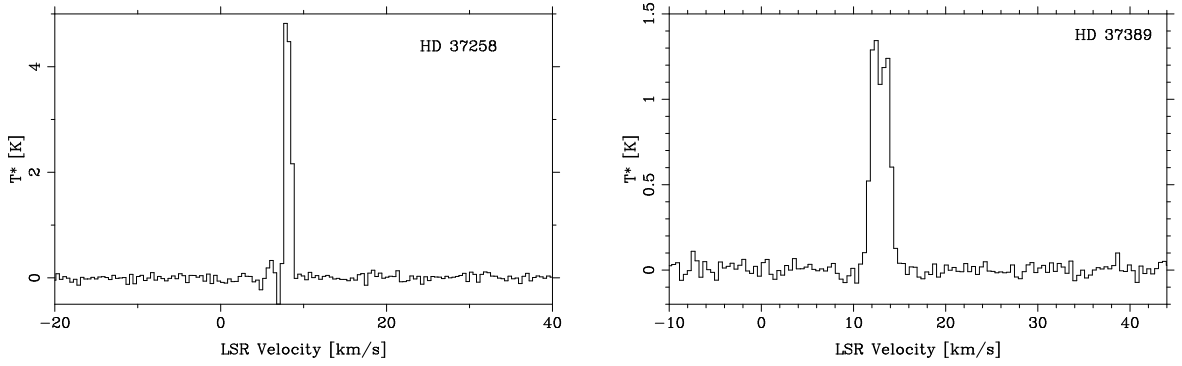


Fig. 16.— Same as Figure 14.

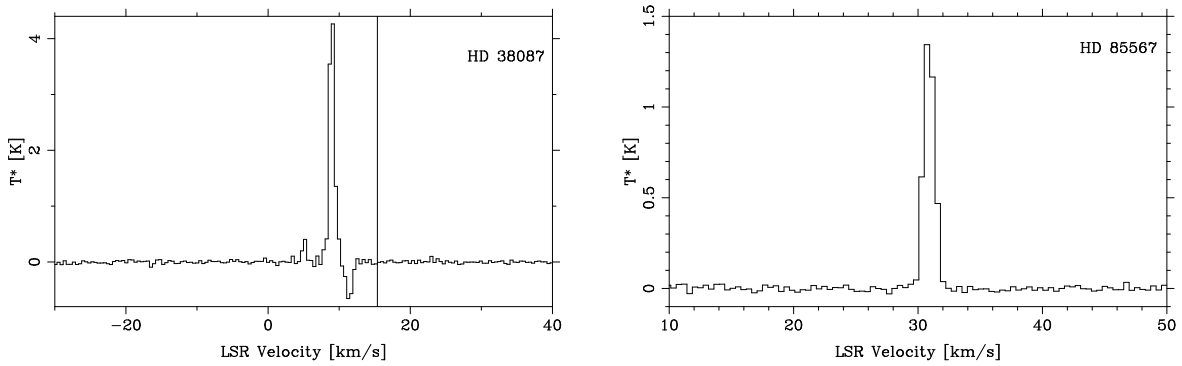


Fig. 17.— Same as Figure 14. The stellar velocity for HD 38087 was obtained from Gontcharov (2007).

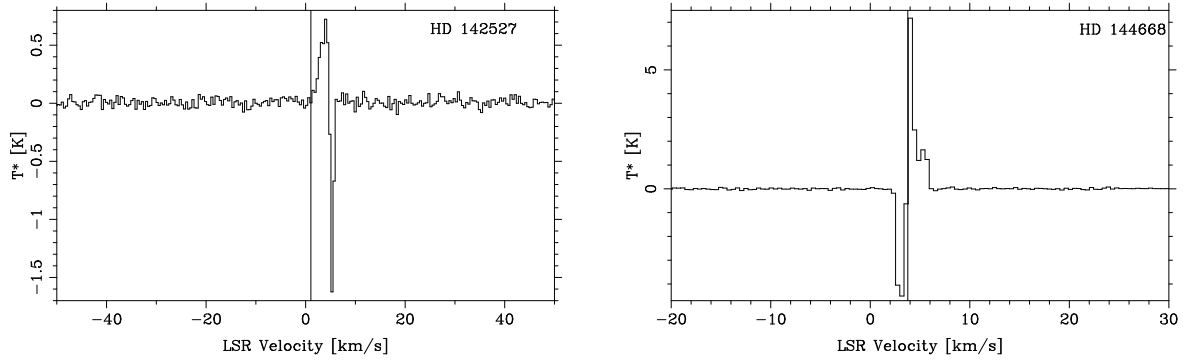


Fig. 18.— Same as Figure 14. The stellar velocity for HD 142527 was obtained from Gontcharov (2007).

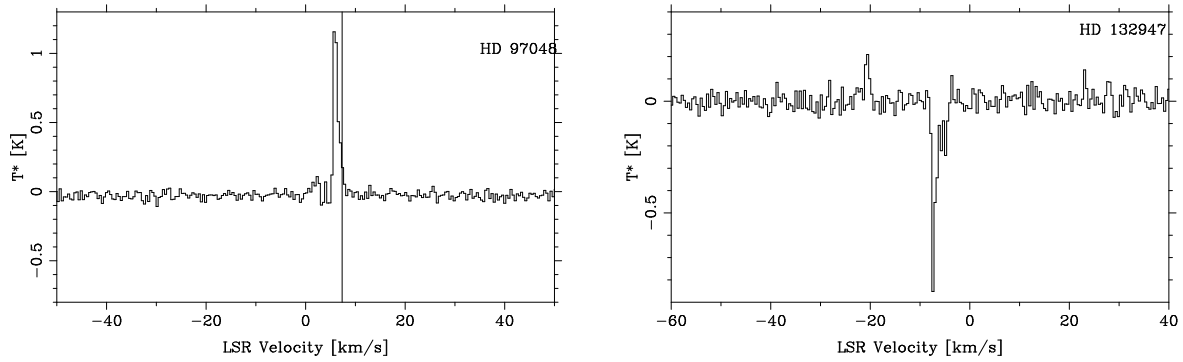


Fig. 19.— Same as Figure 14. The stellar velocity for HD 97048 was obtained from Carmona et al. (2011).

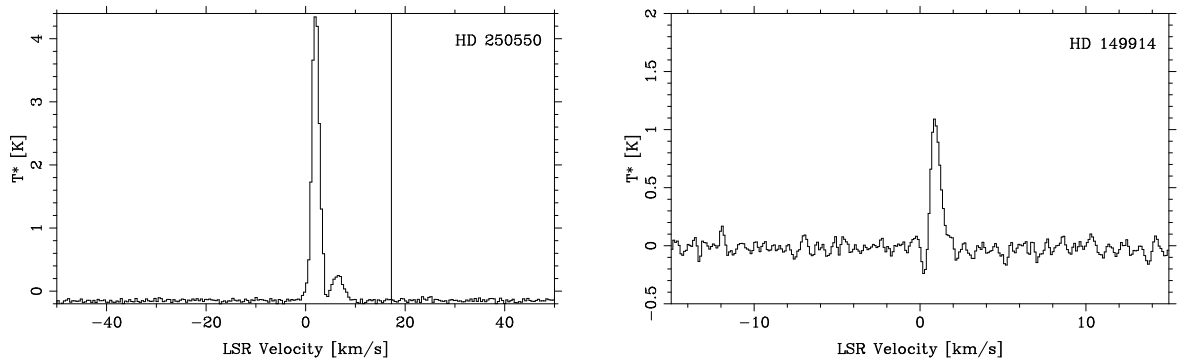


Fig. 20.— Same as Figure 14. The stellar velocity for HD 250550 was obtained from Gontcharov (2007).

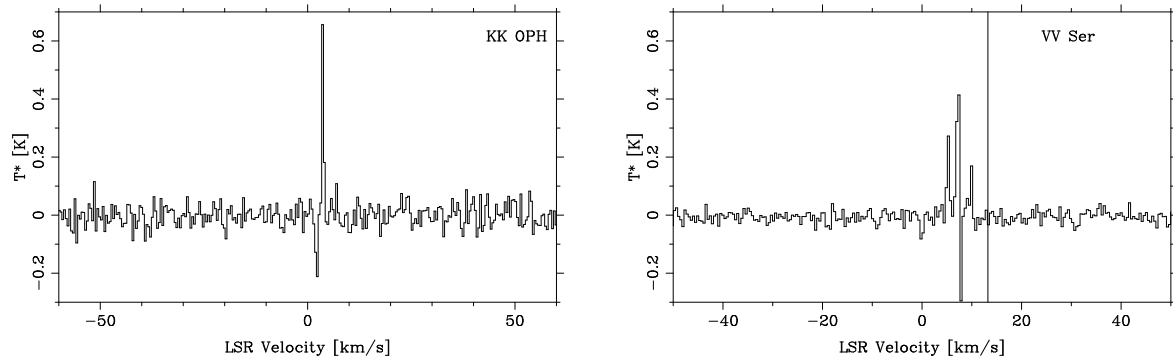


Fig. 21.— Same as Figure 14. The stellar velocity for VV Ser was obtained from Acke et al. (2005)

A.2. CHAMP+ follow up observations

Five sources with $^{12}\text{CO}(3-2)$ detections (HD 142527, HD 178253, HD 37389, RX J1842.9-3532 and VV Ser) were observed with the CHAMP+ dual color heterodyne array at $450\ \mu\text{m}$ and $350\ \mu\text{m}$ with $\sim 8''$ resolution. The 7-horn CHAMP+ receiver allows to map the position of the star and its periphery simultaneously (Güsten et al. 2008), providing a 7-pixel map of the gas emission around each star. The $\text{CO}(6-5)$ 691.4 GHz and $\text{C I}(2-1)$ 809 GHz were targeted in order to confirm the $^{12}\text{CO}(3-2)$ using the $^{12}\text{CO}(6-5)$ line, and the $\text{C I}(2-1)$ to obtain measures of the atomic gas content of the disks. These observations are described in Casassus et al. (2013). Only HD 142527 revealed a compact $^{12}\text{CO}(6-5)$ disk detection, and only $\text{C I}(2-1)$ upper limits. HD 37389 shows clear contamination from extended emission, particularly in the north-eastern horns of the CHAMP+ footprint (Figure 22).

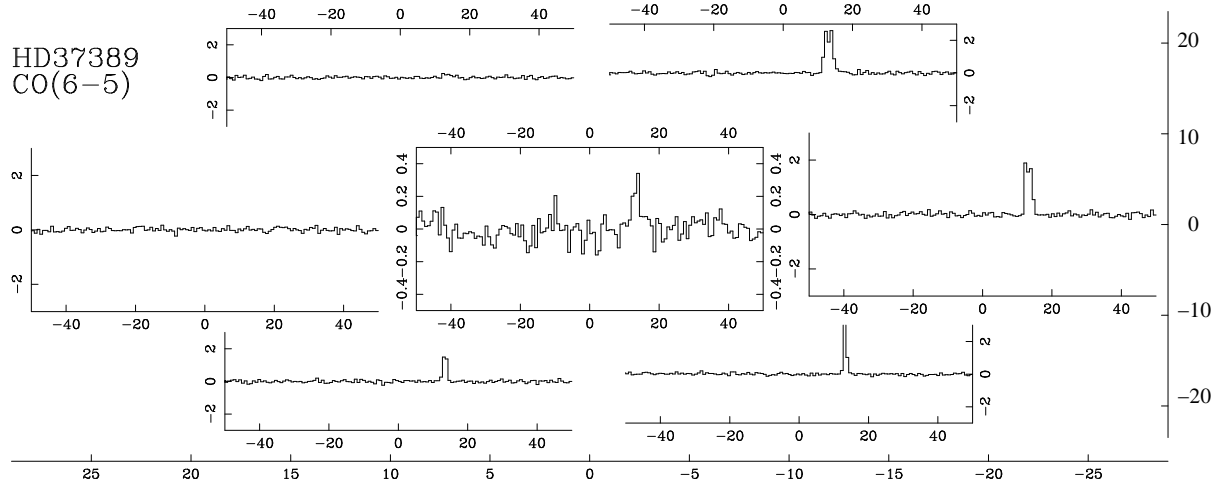


Fig. 22.— CHAMP+ 7-horn footprint for HD 37389 in CO(6-5). The outermost axes show offset RA and DEC, in arcsec. The other axes give T_A^* in y -axis and V_{lsr} is x -axis. The emission from the Orion Molecular Cloud is clearly traced by the CHAMP+ footprint.

